AFRL-MN-EG-TR-1999-7054

PENETRATOR CASE FRACTURE PREDICTIVE TECHNOLOGY: VOLUME II-- NUMERICAL ALGORITHMS AND COMPUTATIONS

G. R. JOHNSON
S. R. BEISSEL
C. E. ANDERSON, Jr,
C. H. POPELAR
J. D. WALKER

Alliant Techsystems Inc.
600 Second Street N.E.
Hopkins, MN 55343

Southwest Research Institute
P. O. Drawer 28510
San Antonio, TX 78228-0510

Approved for public release; distribution is unlimited.

AIR FORCE RESEARCH LABORATORY, MUNITIONS DIRECTORATE

Air Force Materiel Command ■ United States Air Force ■ Eglin Air Force Base
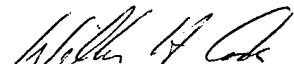
NOTICE

When Government drawings, specifications, or other data are used for any purpose other than in connection with a definitely Government-related procurement, the United States Government incurs no responsibility or any obligation whatsoever. The fact that the Government may have formulated or in any way supplied the said drawings, specifications, or other data, is not to be regarded by implication, or otherwise in any manner construed, as licensing the holder, or any other person or corporation; or as conveying any rights or permission to manufacture, use, or sell any patented invention that may in any way be related thereto.

This technical report is releasable to the National Technical Information Services (NTIS). At NTIS it will be available to the general public, including foreign nations.

This technical report has been reviewed and is approved for publication.

L. Bruce Simpson
Technical Director
Assessments and Demonstrations Division

William H. Cook
Program Manager

If your address has changed, if you wish to be removed from our mailing list, or if your organization no longer employs the addressee, please notify AFRL/MNAC, Eglin AFB FL 32542-6810, to help us maintain a current mailing list.

Do not return copies of this report unless contractual obligations or notice on a specific document requires that it be returned.

REPORT DOCUMENTATION PAGE

1. AGENCY USE ONLY (Leave Blank)	2. REPORT DATE 6/30/99	3. REPORT TYPE AND DATES COVERED Final Report: May 1996 - June 1999

4. TITLE AND SUBTITLE

Penetrator Case Fracture Predictive Technology: Volume 2—Numerical Algorithms and Computations

5. FUNDING NUMBERS

Contract # F08630-96-C-0029

JON: 25020724

6. AUTHOR(S)

G. R. Johnson, S. R. Beissel, C. E. Anderson, Jr., C. H. Popelar, J. D. Walker

7. PERFORMING ORGANIZATION NAME(S) AND ADDRESS(ES)

Alliant Techsystems, Inc.   Southwest Research Institute
600 Second Street, N.E.   P.O. Drawer 28510
Hopkins, MN 44343   San Antonio, TX 78228-0510

8. PERFORMING ORGANIZATION REPORT NUMBER

SwRI Report 18-8037/002

9. SPONSORING/MONITORING AGENCY NAME(S) AND ADDRESS(ES)

Air Force Research Laboratory   Program Manager: Dr. William H. Cook
Munitions Directorate   Phone: 850-882-8302, ext. 3430
101 West Eglin Blvd.
Eglin AFB, FL 32542

10. SPONSORING/MONITORING AGENCY REPORT NUMBER

AFRL-MN-EG-TR-1999-7054

11. SUPPLEMENTARY NOTES

12a. DISTRIBUTION/AVAILABILITY STATEMENT

Approved for Public Release/Unlimited Distribution

12b. DISTRIBUTION CODE

13. ABSTRACT (Maximum 200 words)

The objective of this work was to develop the capability to perform 3D crack propagation computations for penetrator cases during impact and penetration into hard concrete targets. The first step was to develop a new 2D algorithm that did not require rezoning (as rezoning would be very complex in 3D geometry), the second step was to extend the new technique to 3D geometry, and the third step was to apply the 3D algorithm to actual hard target penetrator impact events. The numerical algorithms described in this report have been incorporated into the 1999 version of the EPIC code.

A finite element algorithm is presented for dynamic crack calculations in general directions. The algorithm avoids node splitting and the associated remeshing and redefinition of contact surfaces, and does not rely on failure mechanisms embedded in the constitutive model. The T^* energy integral is employed as the dynamic fracture parameter, guiding the crack tip through the mesh. Elements through which the crack tip passes lose the ability to sustain deviatoric and tensile volumetric stresses, and their interfaces with the rest of the mesh model fractured surfaces that can sustain only compressive normal tractions (when the crack is closed). This technique is therefore referred to as the element-failure algorithm.

14. SUBJECT TERMS

dynamic fracture, fracture mechanics, energy release rate, nodal release, element failure, finite element, EPIC, crack propagation, fracture toughness, crack speed, crack growth, crack driving force

15. NUMBER OF PAGES

46

16. PRICE CODE

17. SECURITY CLASSIFICATION OF REPORT Unclassified	18. SECURITY CLASSIFICATION OF THIS PAGE Unclassified	19. SECURITY CLASSIFICATION Unclassified	20. LIMITATION OF ABSTRACT UL

PREFACE

TABLE OF CONTENTS

LIST OF FIGURES

SECTION 1

INTRODUCTION

This report documents numerical algorithms, numerical examples, and parametric computations for crack propagation in two and three dimensions. Volume 1 of this report presents background information, experimental data, analysis of the data, and computational approaches and results [1]. The numerical algorithms described in this report have been incorporated into the 1999 version of the EPIC code [2].

The objective of this work was to develop the capability to perform 3D crack propagation computations for penetrator cases during impact and penetration into hard concrete targets. The first step was to develop a new 2D algorithm that did not require rezoning (as rezoning would be very complex in 3D geometry), the second step was to extend the new technique to 3D geometry, and the third step was to apply the 3D algorithm to actual hard target penetrator impact events.

Some background on computational approaches for crack propagation is as follows:

Finite element modeling of fracture propagation has traditionally been achieved by splitting nodes along a crack path and allowing the adjacent elements to separate. If there are no symmetry assumptions and the crack is allowed to propagate in any direction, remeshing algorithms become necessary; examples of such algorithms appear in [3, 4, 5, 6]. If a plane of symmetry is assumed — as is often the case when the study does not focus on the direction of crack propagation — the node-splitting technique reduces to a "node-release" technique in which the propagating crack is modeled by the release of restrained nodes along the line of symmetry. Examples of this type appear in [7, 8, 9]. In the node-release technique, external forces are typically applied to the nodes immediately after they are released. These forces are then reduced to zero as the crack tip traverses the element edge, reducing the waves generated by a sudden release of restraint and extracting energy. For both the node-splitting and node-release techniques, a fracture criterion (in conjunction with an energy integral or the crack-tip opening angle) must be employed to determine the speed of propagation. For the node-splitting technique (in general directions), a criterion to determine the direction of propagation must also be employed.

1

As an alternative to the node-splitting technique, micromechanically based approaches have been proposed in which the speed and direction of propagation are determined directly from the constitutive models via material failure. Examples of these approaches appear in [10, 11]. To elaborate on a specific example, Needleman and Tvergaard [10] use an elastic-viscoplastic constitutive relation for a porous plastic solid, which models the nucleation and growth of voids to coalescence. They demonstrate a loss of convergence of a dynamic J-integral with mesh refinement when a void-size length scale is omitted from the constitutive relation. An advantage of the micromechanically based approaches is the relative ease with which the crack model is propagated through the mesh; remeshing and modifying contact surfaces are not necessary.

Dynamic fracture has also been modeled by means other than finite elements, e.g., the boundary element (BE) method and the element-free Galerkin (EFG) method. Belytschko et al [12, 13, 14] use the EFG method, in which the spatial discretization consists only of nodes, and shape functions are generated by a moving least-squares approximation of the nodal data. This method allows the advancing crack to be modeled by simply modifying the nodal connectivities. Energy integrals are used as fracture parameters.

In this report, a finite element algorithm is presented for dynamic crack calculations in general directions. The algorithm avoids node splitting and the associated remeshing and redefinition of contact surfaces, and does not rely on failure mechanisms embedded in the constitutive model. The T* energy integral is employed as the dynamic fracture parameter, guiding the crack tip through the mesh. Elements through which the crack tip passes lose the ability to sustain deviatoric and tensile volumetric stresses, and their interfaces with the rest of the mesh model fractured surfaces that can sustain only compressive normal tractions (when the crack is closed). This technique is therefore referred to as the element-failure algorithm. Discussions of crack-tip energy integrals leading to the development of T* appear in Atluri et al [15] and Nakamura et al [16]. The development of T* appears in Atluri et al [17, 18].

The following three sections provide a description of the 2D algorithm, a description of the 3D algorithm, and a computational parametric study for a hard target penetrator.

SECTION 2

2D ALGORITHMS

2.1 THE 2D ELEMENT-FAILURE ALGORITHM

Figure 1 demonstrates a typical remeshing technique used with a node splitting algorithm. The region of the mesh near the crack tip is remeshed as the tip moves through the mesh, allowing propagation in any direction. Remeshing entails optimizing the new mesh, modifying the nodal connectivites accordingly, and mapping state variables from the old mesh to the new one. The new crack surfaces are then incorporated into the contact algorithm.
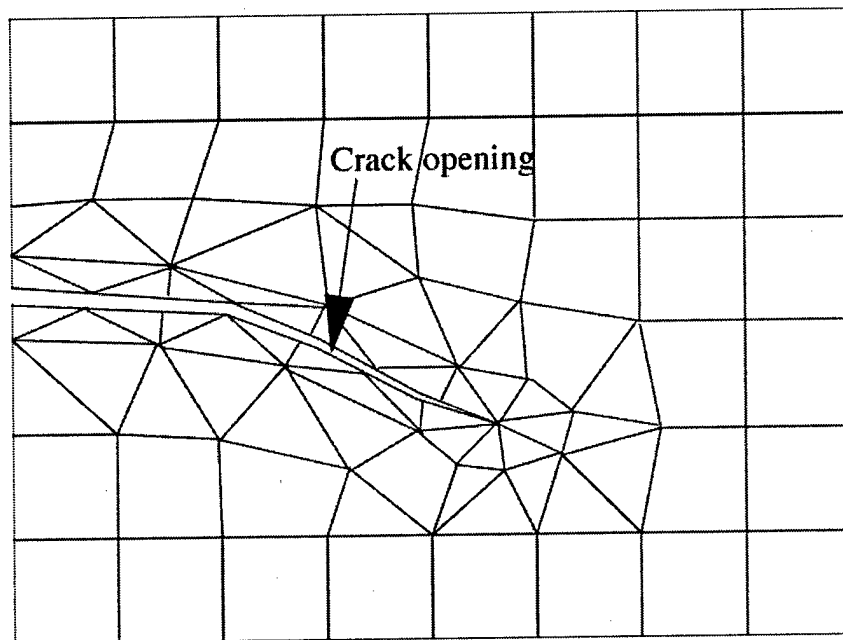
Figure 1. Example of a Remeshing Technique in a Node-splitting Algorithm [01_T103794.tif]

In the element-failure algorithm of Figure 2, a criterion for the direction of propagation is invoked each time the crack tip enters a new element. (The tip is restricted to traveling in a straight line through the element.) After the direction has been determined, the fracture parameter T*, when combined with a fracture criterion, determines the speed of propagation. T* is recalculated at each timestep, and the tip speed is subsequently updated. The elements through which the tip passes lose the ability to sustain deviatoric and tensile volumetric stresses; i.e., they are failed. This technique requires no remeshing, and none of the associated optimization and mapping. The failed elements (shaded in Figure 2) can sustain only positive pressure, and this

Failed elements (shaded)   Cracktip path
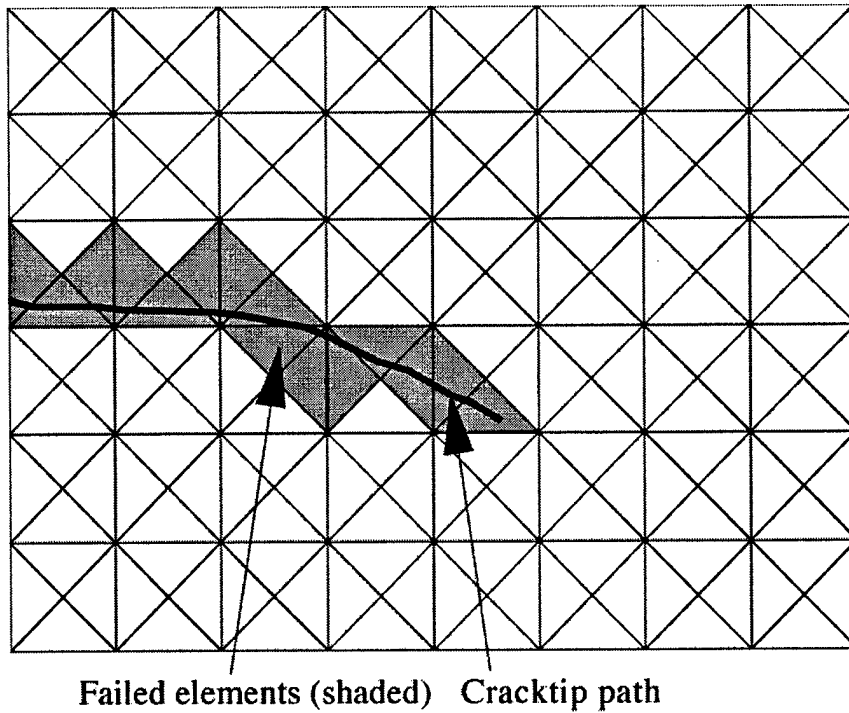
Figure 2. Crack Path Model of the Element-failure Algorithm [02_T103794.tif]

typically occurs under negative volumetric strains. An edge between a failed and an unfailed element therefore acts as a traction-free crack face when the volumetric strain of the failed element is positive (opened crack), and a pressure-transmitting crack face when the volumetric strain of the failed element is negative (closed crack). Crack-face surfaces are not incorporated into the contact algorithm.

If a crack path falls along a plane of symmetry, a node-splitting algorithm may be reduced to a node-release algorithm. The left side of Figure 3 shows how, in a node-release algorithm, the advancing crack is modeled by the release of nodes which were restrained in the x-direction along the line of symmetry. The sudden release of these nodes generates release waves (noise), an effect that is often avoided [7, 8, 9] by replacing the x-restraint with an externally applied nodal force. This force, denoted by P on the left side of Figure 3, is effectively equivalent to the restraint, but it is subsequently reduced to zero as the crack tip moves toward the next node along the line of symmetry. This technique is used for the node-release calculations reported in subsection 2.3.1.
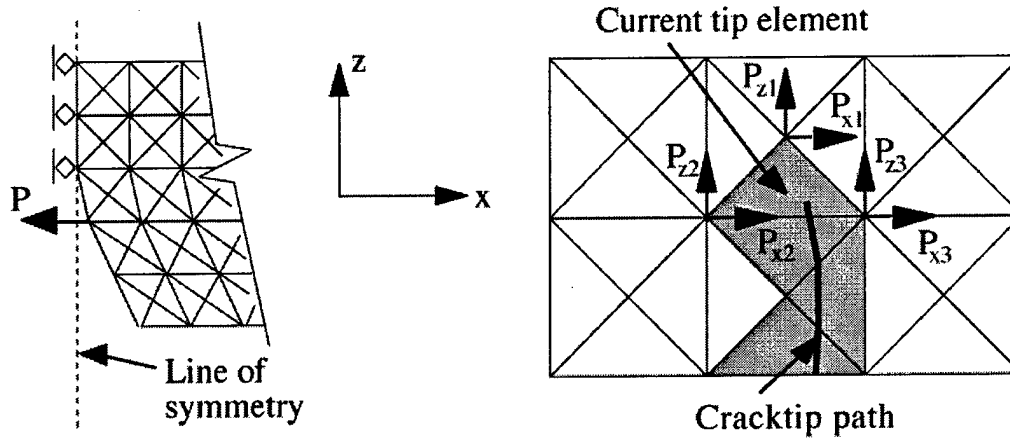
Figure 3. Release Forces in Node-release Algorithm (left, P) and Element-failure Algorithm (right, P_{x1}, P_{z1}, ..., P_{z3}) [03_T103794.tif]

For the element-failure algorithm, the right side of Figure 3 shows the manner in which release forces are used to avoid the release waves associated with the sudden failure of the current crack-tip element. When the crack tip first enters the element, the element is failed and external forces (P_{x1}, P_{z1}, ..., P_{z3} in Figure 3) are applied to all the nodes of the failed element. The external forces are equivalent to the internal forces on those nodes due to the stresses in the element before it was failed. As in the node-release algorithm, the release forces are subsequently reduced to zero as the crack tip moves through the element. They vary linearly to zero as the tip reaches a distance of $\sqrt{2\,A_{ele}}$ from its location when the forces were initially applied. (A_{ele} = current area of the element.) Shorter values of this distance were found to generate significantly more noise in the solution.

2.2 THE T* FRACTURE PARAMETER

As a measure of the energy release associated with a unit area of crack surface extension in dynamic fracture, T* [17, 18] is expressed as,

$$T^* = \lim_{\Gamma^* \to 0} \int_{\Gamma^*} \left[\left(\overline{W} + T \right) n_p - \sigma_{ij} n_j u_{i,p} \right] d\Gamma^* \tag{1}$$

where Γ^* is a line contour around the crack tip. $\overline{W}$ and T represent the internal energy density and kinetic energy density, respectively; σ_{ij}, the ij-th component of the stress tensor; n_j, the j-th component of the unit normal vector to Γ^*; n_p, the component of the unit normal vector in the direction of crack propagation; u_i, the i-th component of the displacement vector; $u_{i,p}$, the

derivative of the i-th component of the displacement vector in the direction of crack propagation. (Note p is not a free subscript.)

The largest errors in a numerical solution occur in the region of the crack tip, where field quantities vary most rapidly. As a result, it is desirable to equate the limiting integral of Equation 1 to area and contour integrals by the divergence theorem [7],

$$T^* = \int_\Gamma \left[\left(\overline{W} + T \right) n_p - \sigma_{ij} n_j u_{i,p} \right] d\Gamma - \int_\Omega \left[\left(\overline{W} + T \right)_{,p} - \rho \ddot{u}_i u_{i,p} - \sigma_{ij} \left(u_{i,j} \right)_{,p} \right] d\Omega \qquad (2)$$

where Γ represents a large crack-tip contour and Ω is the area between Γ and Γ^*. A subscript following a comma represents the direction of a spatial derivative.

For the computations of this study, meshes were constructed of constant-strain triangles in the "crossed" configuration. Figure 4 shows how Γ^*, Γ and Ω can be arranged around a crack tip and its associated failed elements in a crossed-triangle mesh. While the definition of T^* in Equation 1 is the near-field integral around Γ^*, its calculation is achieved by the far-field integral around Γ and the area integral over Ω. The segments of Γ^* in Figure 4 are not used in this calculation.
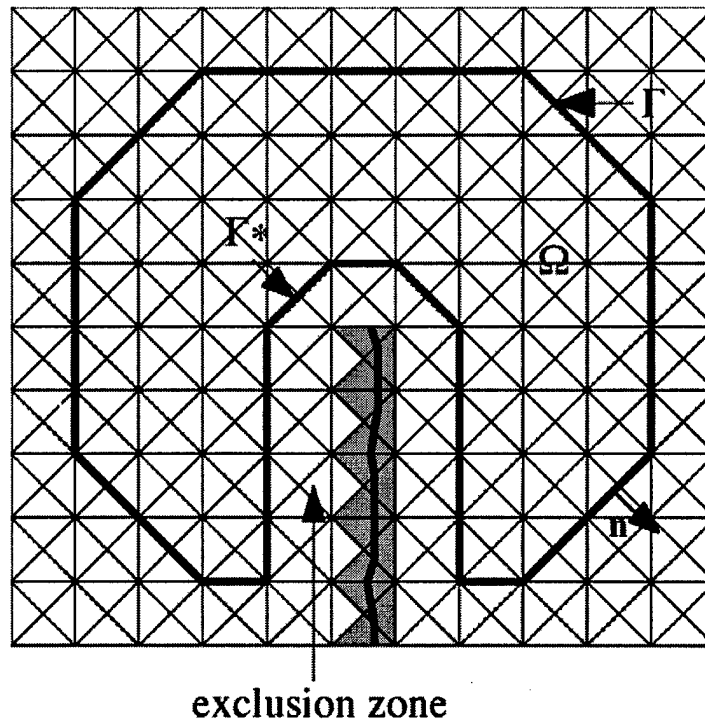

Figure 4. Domains of Integration in the Calculation of T* [04_T103794.tif]

For each triangular element, the displacement is interpolated linearly, resulting in constant displacement derivatives, stresses, densities, and internal energy densities. Numerical integration of the integral over Γ in Equation 2 is achieved by the trapezoidal rule applied to each of the boundary segments in counterclockwise order. This scheme requires nodal values of the integrand, which includes the internal and kinetic energy densities, the stresses, and the displacement derivatives. To generate nodal values of these quantities, values from adjoining elements are averaged at the nodes.

The integral over Ω in Equation 2 is integrated by employing one-point quadrature over each triangular element in Ω. For constant-strain triangles, the second-order displacement derivatives must be smoothed before application of the quadrature scheme (because they are zero in the interiors of the elements and infinite at the element boundaries). Smoothing is achieved by averaging values of the first displacement derivatives from the adjoining elements at each node, and then interpolating those nodal values linearly over each element to render constant second displacement derivatives in each element. A similar approach is used for the energy-density derivatives. Dexter and O'Donoghue [8] also use a node-averaging technique to smooth the internal energy and strain derivative fields, and they report greatly improved accuracy in the computed values of T*.

Since the limit in Equation 1 cannot be taken in a numerical solution, it is necessary to use an inner contour, Γ^*, of finite size. The use of the divergence theorem to generate Equation 2 is motivated by the greater accuracy of the finite element solution in the far-field region than in the near-field region.

It has been reported [8] that a lack of convergence with mesh refinement occurs for solutions of ductile fracture if Γ^* is taken at the limit value of zero. In subsection 2.3.2, it will be shown that a finite value of Γ^* is necessary for convergence. It is also recommended [7, 8] that all elements that have been inside Γ^* be excluded from Ω in subsequent evaluations of T* due to the lack of accuracy of the numerical solution in the crack tip region and the continuation of those errors when path-dependent materials (plasticity) are unloaded. The result is a zone of elements that are not included in Ω forming a wake behind the crack tip. This exclusion zone is depicted in Figure 4, and its effect is a modification of the shape of Γ^*. In this report, the size of the exclusion zone will be reported by a radius, and all elements whose centroids have been, at any time, within that radius of the crack tip will be excluded. In a similar manner, the size of the outer contour Γ will be reported by a radius, and the edges of the elements whose centroids

currently lie within that radius of the crack tip and outside the exclusion zone will determine Γ. The domain Ω is defined by the region contained inside the closed contour $\Gamma + \Gamma^*$.

2.3 NUMERICAL RESULTS

Both the 2D and 3D algorithms have been incorporated into the 1999 version of the EPIC Code [2], which is based on an explicit dynamic displacement-based finite element formulation [19]. The equations of motion are integrated by central differences and the coupled equations of crack propagation are integrated by the forward-Euler scheme. All 2D calculations were performed in plane strain.

For the element-failure calculations, no assumptions are made on the direction of propagation due to symmetry. The direction may be chosen perpendicular to the direction of the maximum normal stress in the region of the crack tip, implying mode one fracture, or as that which produces the largest value of T*, allowing mixed-mode fracture. Because this formulation does not require the generation of a stiffness matrix, the nonlinearities are treated in an explicit manner, and many of the difficulties associated with zeroing stiffness terms are avoided.

2.3.1 Comparison of Element Failure and Node Splitting

The primary advantage of the element-failure method is the simplicity of implementation — there is no need for remeshing or redefining contact surfaces. The accuracy of the method, however, can be gauged by a comparison of results to the prevalent node-splitting method. The sample problem used for comparison is the coupled pressure-bar specimen of Figure 5 under dynamic loading. The material model is elastic/perfectly plastic with the von Mises flow rule $\sqrt{3J_2} = \sigma_y$. The material parameters are intended to represent a steel: elastic modulus, E = 200 GPa; Poisson's ratio, v = 0.3; and uniaxial yield stress, σ_y = 1.1 GPa. The fracture response is prescribed by the resistance, $R(v_c)$, a function of tip velocity, and it is plotted on the right side of Figure 5. This resistance exhibits a very strong dependence on crack speed, and it was selected to produce substantial crack-tip plasticity. For values of T* less than the threshold value of $R(v_c = 0)$ = 20 kN/m, the crack tip velocity v_c is zero. For values of T* above the threshold, the resistance increases linearly and T* = $R(v_c)$ determines the tip velocity. The loading is a prescribed velocity that increases linearly with time,

$$v_x = \alpha_v t \tag{3}$$

where $\alpha_v = 110,000 \text{ m/s}^2$; see Figure 5.
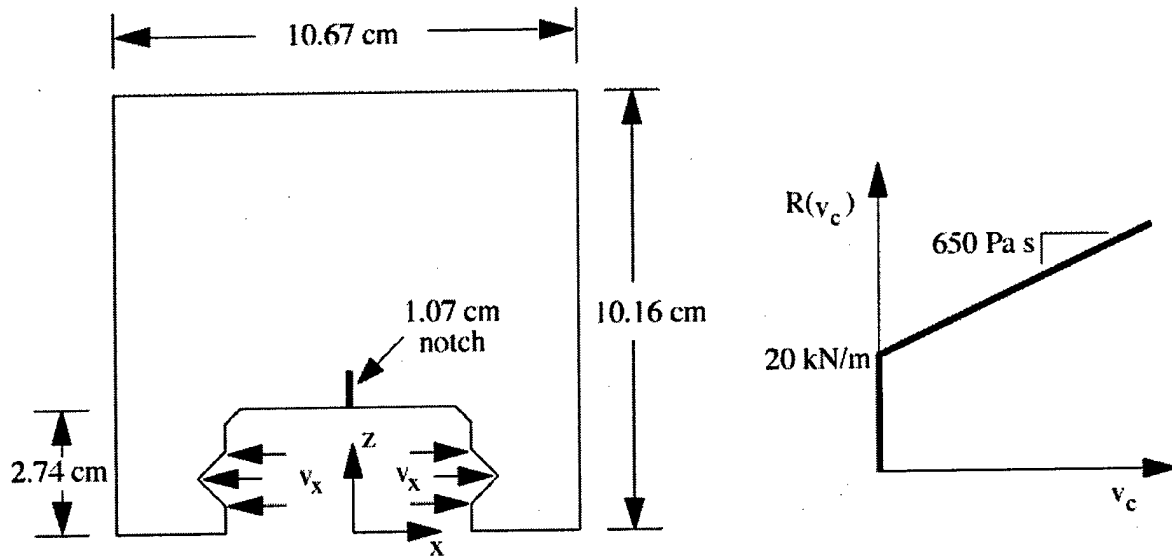
Figure 5.   Coupled Pressure-bar Specimen and Fracture Response Function
[05_T103794.tif]

Symmetry along the crack path allows for use of the node-release algorithm. Its mesh is shown on the left side of Figure 6, and contains 1419 nodes and 2720 elements. For the element-failure algorithm, a full mesh of 2862 nodes and 5536 elements is used, as shown on the right side of Figure 6. For both algorithms, the radius of Γ is 1.5 cm and the radius of Γ^* is 0.5 cm.
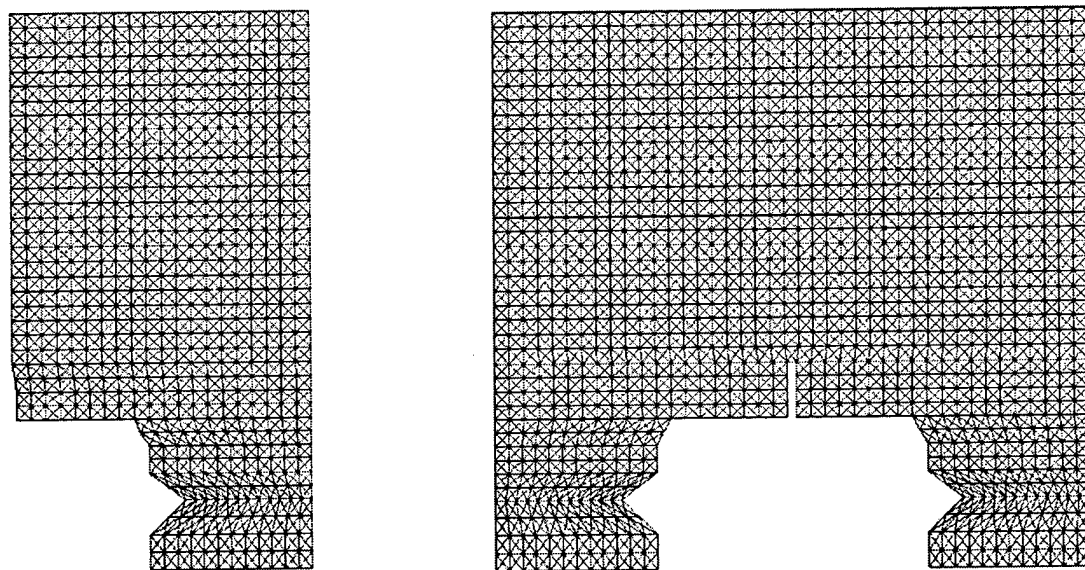
Figure 6.   Meshes for Comparison of Node-release (left, 2720 elements) and Element-failure (right, 5536 elements) Methods [06a/b_T103794.tif]

Figure 7 contains plots of T* and the z-coordinate of the crack tip as functions of time for both the node-splitting and element-failure methods. Close agreement indicates similar accuracy of the two methods. Figure 8 is a plot of the mesh at 250 μs, with the failed elements shaded. This plot verifies adequate performance of the propagation-direction criterion.
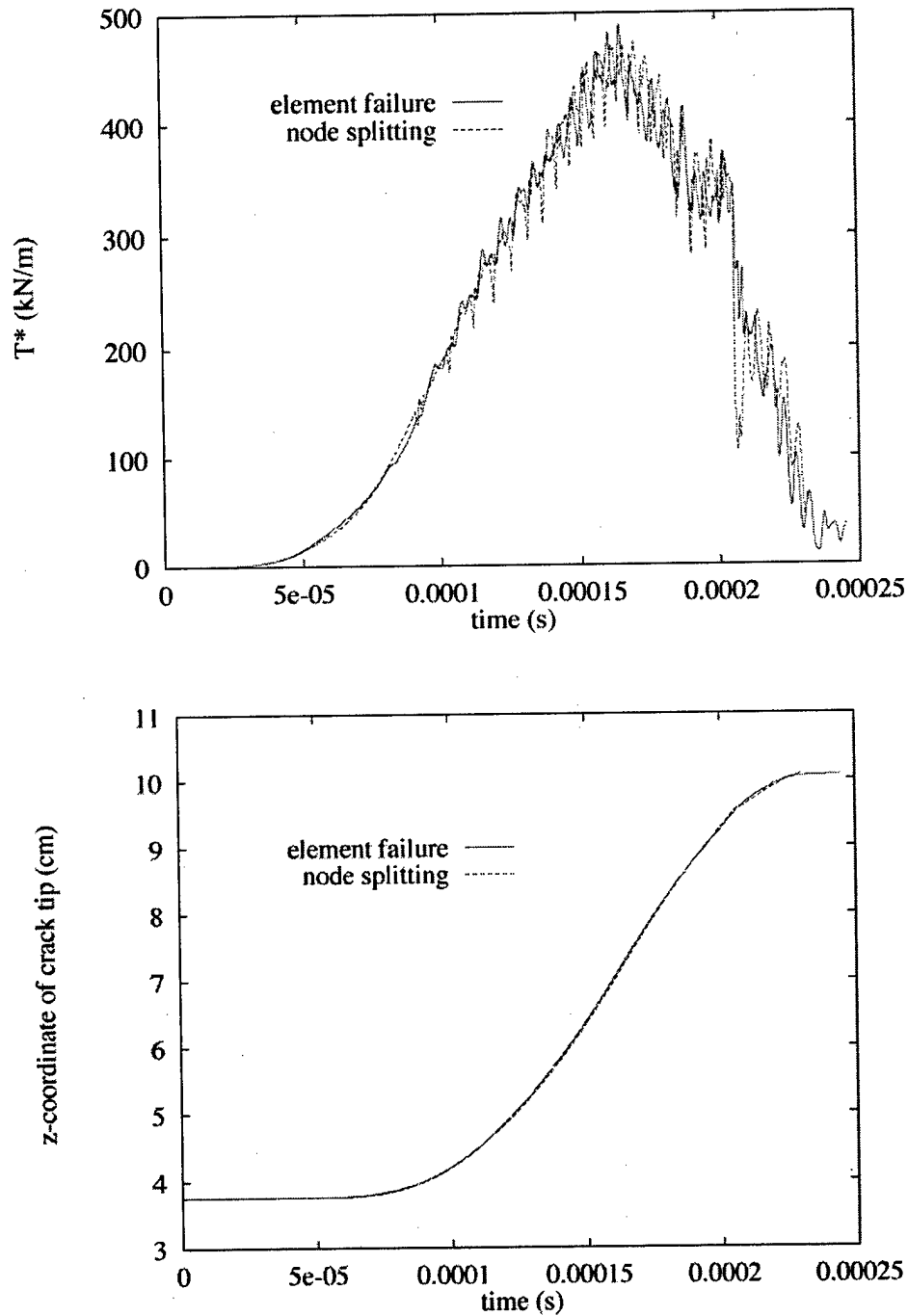
Figure 7.   Comparison of Results for Node-release and Element-failure Methods
[07a/b_T103794.tif]
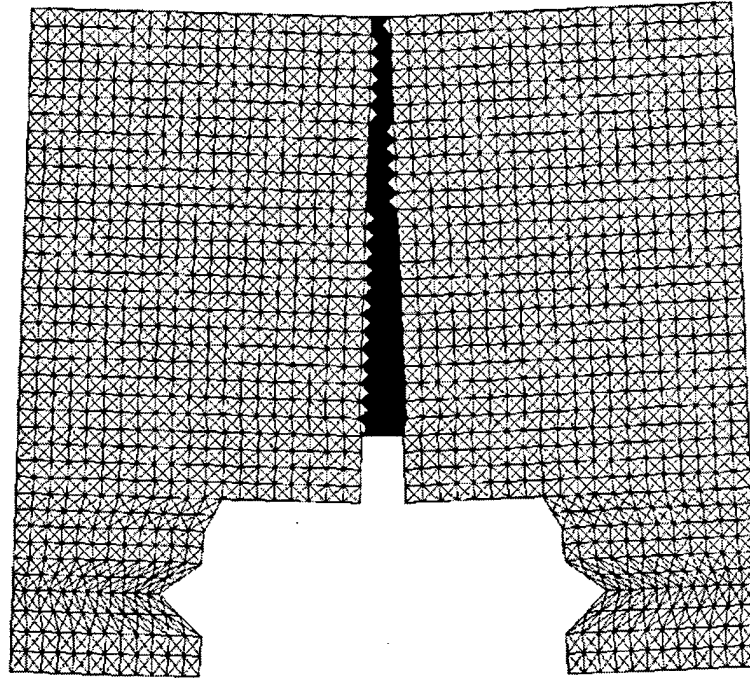
Figure 8. Element-failure Mesh at 250 μs (failed elements shaded) [08_T103794.tif]

The large drop in the value of T* in Figure 7 around 210 μs is a result of the crack approaching the top surface of the specimen. When the distance from the crack tip to a surface is shorter than the radius of Γ*, as depicted in Figure 9, a segment of Γ* will coincide with a segment of Γ. The effect of this coincident segment is the loss of the contribution of that segment to the computed value of T*, and a corresponding reduction in the speed of the crack tip, which can be seen as a change in slope of the plot of the z-coordinate of the crack tip versus time in Figure 7.
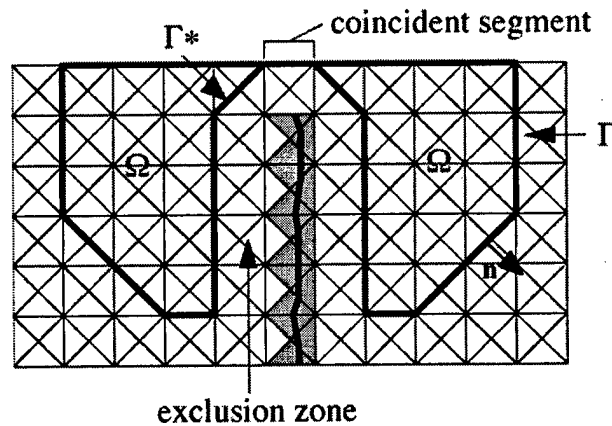
Figure 9. Domains of Integration Near a Surface [09_T103794.tif]

2.3.2 Convergence of T*

In this section, the sample problem of subsection 2.3.2 is used to study the convergence characteristics of the T* fracture parameter with mesh refinement. It has been shown [7, 8] that the node-release algorithm converges for a constant radius of Γ*. Brust et al [7] conclude that the radius of Γ* should be chosen small enough so that the crack-tip fields are captured, and large enough to avoid the relatively large errors in the finite element approximation of the fracture process zone. These findings are verified here, and similar calculations are made for the element-failure method.

The meshes used in the node-release convergence study contain 370 nodes and 680 elements (coarse), 1419 nodes and 2720 elements (medium), and 5557 nodes and 10,880 elements (fine). For the element-failure study, they contain 728 nodes and 1361 elements (coarse), 2862 nodes and 5536 elements (medium), and 11,162 nodes and 21,952 elements (fine). The medium meshes are those of Figure 6, and their element edge lengths are approximately one-half those of the coarse meshes. Likewise, the element edge lengths of the fine meshes are one-half those of the medium meshes.

The top of Figure 10 is a plot of T* versus time for each of the three meshes using the node-release method with a zero radius of Γ*. The bottom of Figure 10 is the same plot with a radius of Γ* of 0.5 cm. Convergence is evident when the radius is nonzero, but lacking when it is zero. These results verify the need to use a finite value of the radius in computations. The limit value of zero in the definition of Equation 1 renders nonconvergent values of T*.

The same comparison can be made for the element-failure algorithm. The top of Figure 11 is a plot of T* versus time for each of the three meshes, using the element-failure method with a zero radius of Γ*. The bottom of Figure 11 is the same plot using a radius of 0.5 cm. As was the case for the node-release method, T* converges for the nonzero value of the radius of Γ*, but does not when the radius is zero. Similar behavior is obtained from the node-release and element-failure methods, indicating that the cause of divergence for a zero radius of Γ* is not a characteristic of the crack-propagation routine (node-release or element-failure).

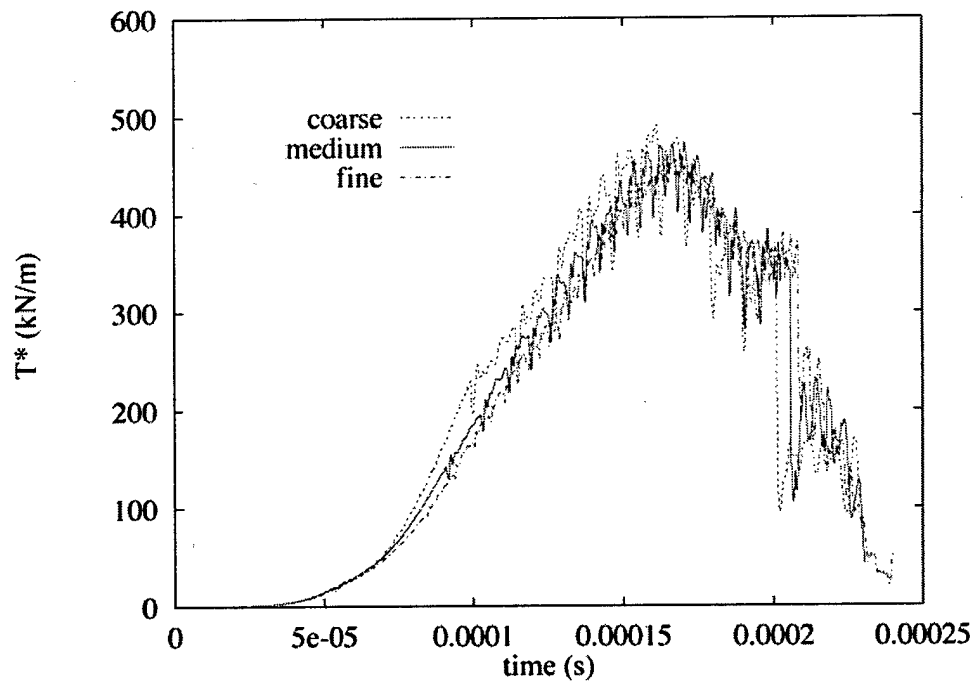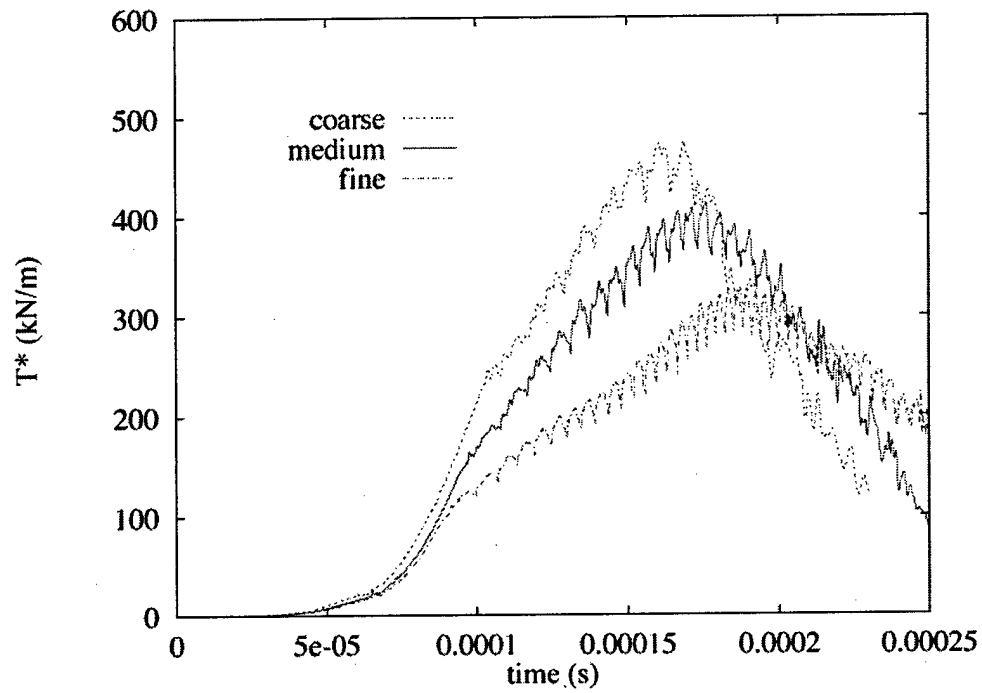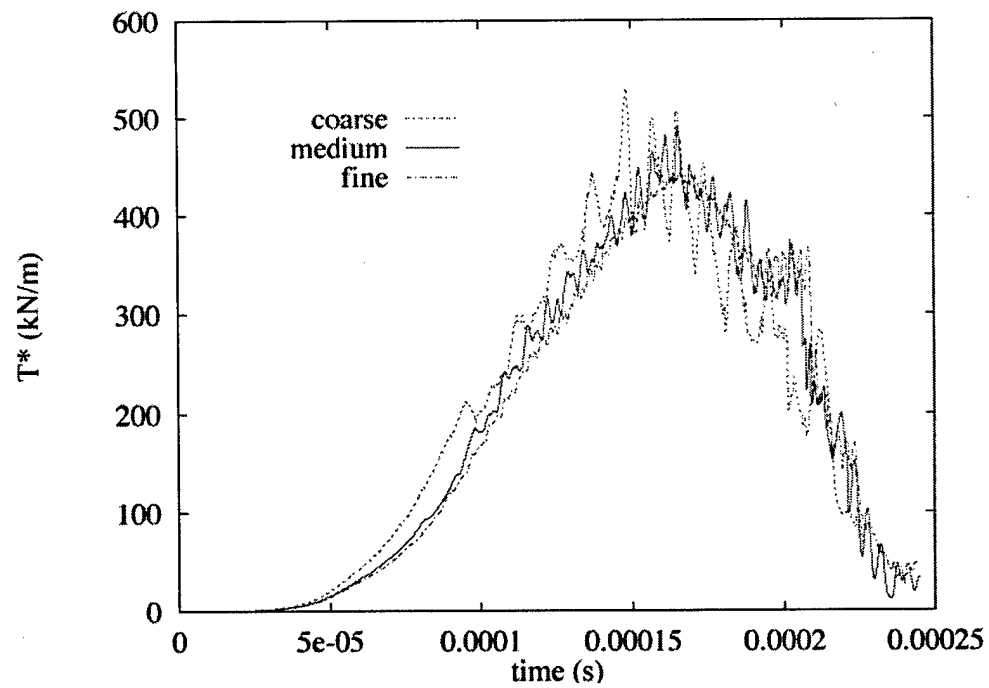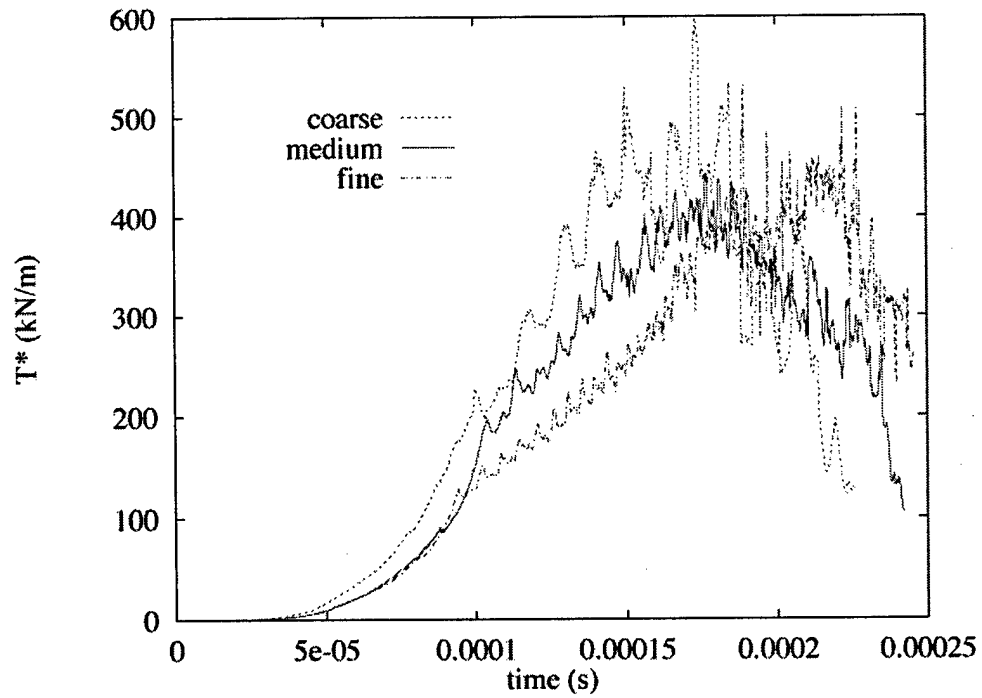**Figure 10. T* Versus Time with Mesh Refinement for Node Release and Radius of
Γ* of Zero (top) and 0.5 cm (bottom)** [10a/b_T103794.tif]

13

Figure 11. T* Versus Time with Mesh Refinement for Element Failure and Radius of Γ* of Zero (top) and 0.5 cm (bottom) [11a/b_T103794.tif]

While the definition of T^* in Equation 1 includes the limit as Γ^* goes to zero, it is apparent by the demonstrated lack of convergence that this limit cannot be achieved by simply using a zero radius of Γ^* in finite-element modeling. It therefore remains to choose an optimal nonzero value of this radius. Since the energy absorbed by the plastic deformation of elements in the exclusion zone is erroneously attributed to the crack tip (for the formation of new crack faces) and included in the calculated value of T^*, it is desirable to minimize the nonzero radius of Γ^*. Therefore, a recommended value of this radius is that which excludes from Ω only the first layer of elements around the crack tip. Additionally, the size of the elements around the crack tip should be small in relation to the size of the plastic zone.

To determine the sensitivities of the T^* calculations in the coupled pressure-bar specimen of this section, the medium mesh on the right side of Figure 6 is used in a parametric study of the radii of Γ and Γ^*. The top of Figure 12 shows plots of T^* versus time for three values of the radius of Γ^*: 0.25, 0.50, and 0.75 cm. (The radius of Γ is 1.50 cm.) The value of 0.25 cm is chosen to represent the smallest value that effectively differs from zero, inasmuch as it excludes the first layer of elements next to the crack tip. The value of 0.50 cm is that used in the previous convergence study. The value of 0.75 cm excludes three to four layers of elements around the crack tip. The differences in these plots are an indication of the size of the complimentary errors due to the inability of the mesh to resolve the crack tip fields and the erroneous contribution of plastic work in Γ^* to the crack tip. By comparison, the bottom of Figure 12 shows plots of T^* versus time for three values of the radius of Γ: 1.0, 1.5, and 2.0 cm. (The radius of Γ^* is 0.50 cm.) The value of 1.0 cm ranges from four to six layers of elements around the crack tip. Since there is no reference to Γ in the definition of T^*, valid numerical approximations should not be sensitive to its size. For this example with substantial crack-tip plasticity, the calculated values of T^* appear relatively insensitive to changes in the size of both Γ and Γ^*.

2.3.3 Off-centered Notch

The advantages of the element-failure method lie in the ease with which it models crack propagation in general directions. In this section, the coupled pressure-bar specimen of subsection 2.3.1 is modified so that the notch is no longer centered between the grips. The mesh, shown at the top of Figure 13, contains the same number of nodes and elements as the medium mesh of subsection 2.3.2. The loading and material characterization are unchanged.
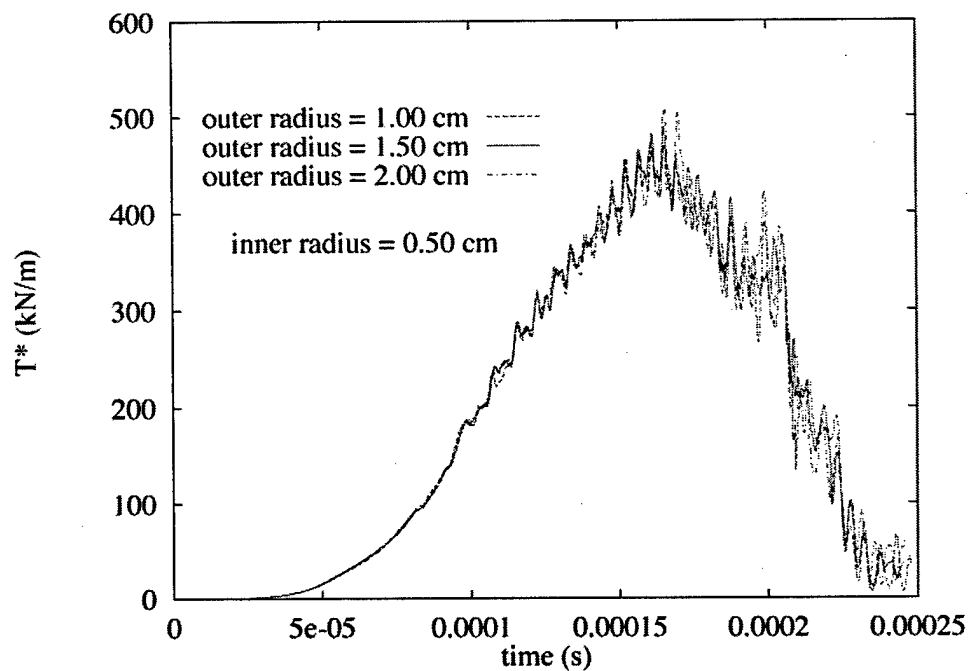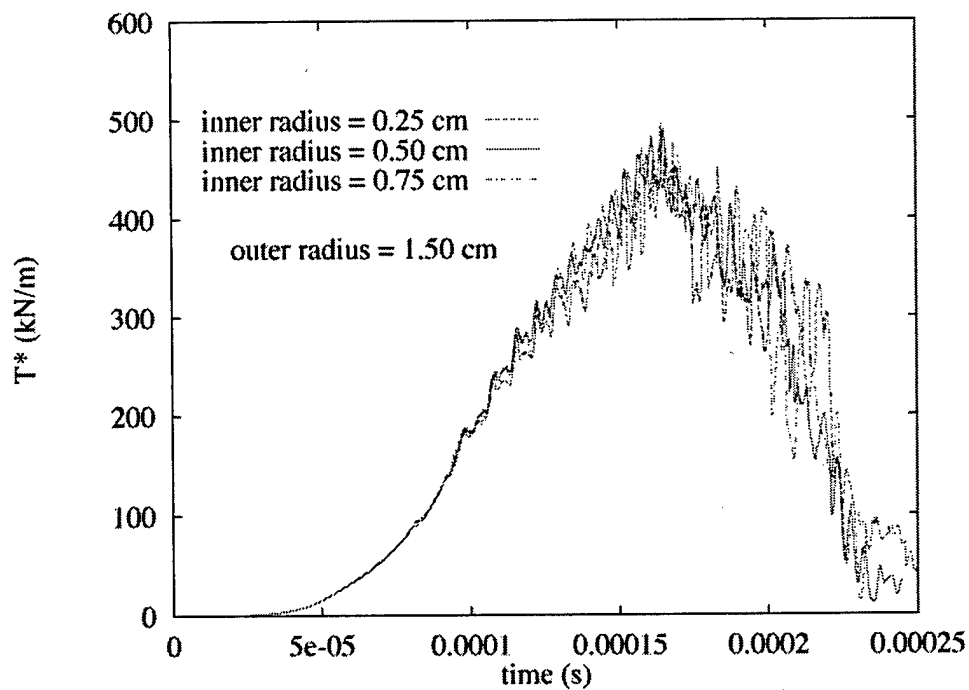
Figure 12. **T* Versus Time for Three Radii of Γ* (Top) and Three Radii of Γ (Bottom)** [fig12top/bottom.T103794.tif]
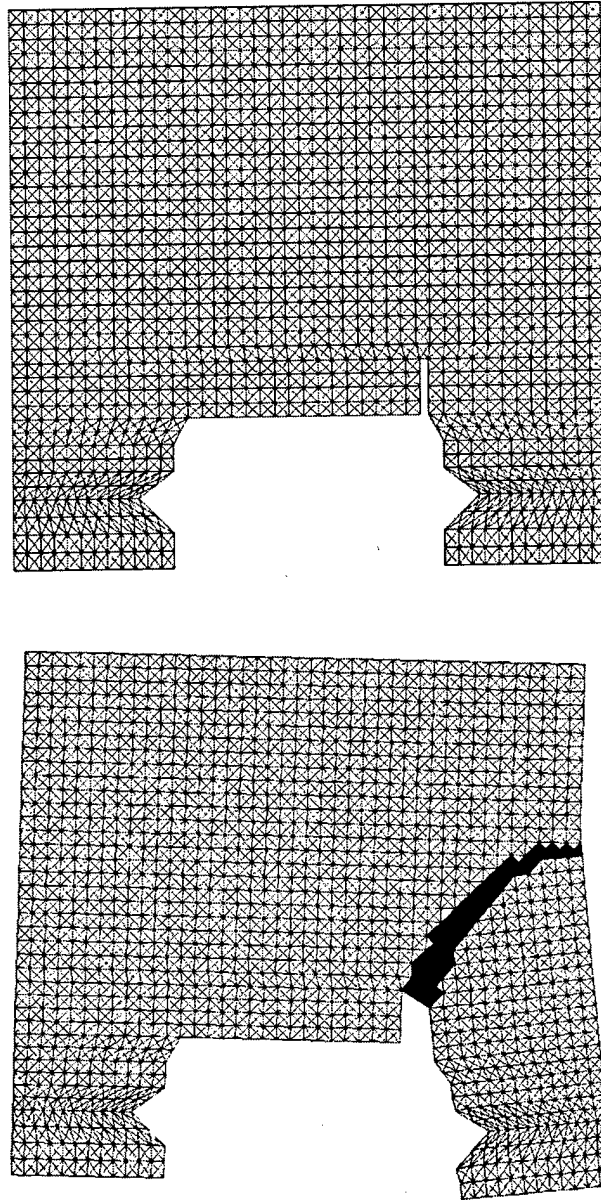
Figure 13. Off-centered Notch Meshes at 0 µs (top) and 250 µs (bottom, failed elements shaded) [12a/b_T103794.tif]

The bottom of Figure 13 displays the mesh at 250 µs, with the failed elements shaded. Here the direction of propagation was determined by the direction of maximum T*. These calculations were also performed with the direction of propagation perpendicular to the maximum normal stress in the region of the crack tip, again resulting in a crack path that veers toward the free surface on the right side of the specimen. These calculations demonstrate the ability of the element-failure method (including the direction-determination criterion) to model the propagation of curved cracks.

2.3.4 Interior Crack

The preceding calculations of coupled pressure-bar specimens rely on a notch to produce stress concentrations from which cracks are generated. The element-failure method also provides a convenient method for modeling interior cracks that are generated from a material flaw. The flaw can be simulated by failing an element prior to loading. Multiple crack tips can then be allowed to propagate from the flaw, as long as the domain Ω, used to calculate T* for one tip, does not capture another tip. Figure 14 demonstrates how the contours can be drawn for the two tips of an interior crack. Note that the domains may overlap.
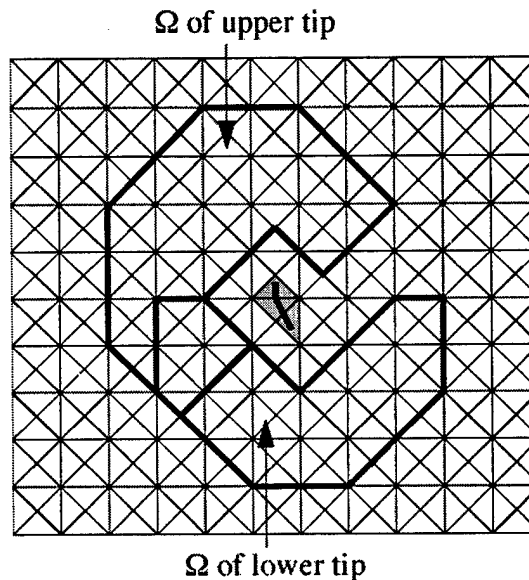
Figure 14. Domains of Integration for Interior Crack [13_T103794.tif]

A sample calculation of an interior crack has been performed on a rectangular block of 4982 nodes and 9760 elements. The block measures 10 by 15 cm and the material model is identical to that of subsection 2.3.1. The block is put in tension by applying the loading of Equation 3 to both ends.

Figure 15 shows the meshes at 150 μs (top) and 200 μs (bottom). The initial flaw is modeled by one failed element adjacent to the centerline. Two crack tips subsequently propagate in opposite directions (up and down) perpendicular to the tensile stress field, as determined by the direction of maximum T*. Due to symmetry, an exact solution would indicate identical values of T* and tip velocity for both crack tips. The finite element solution of this demonstration produces the values of T* for the two tips plotted in Figure 16, with the degree of agreement suggesting the ability of the element-failure method to model interior cracks.
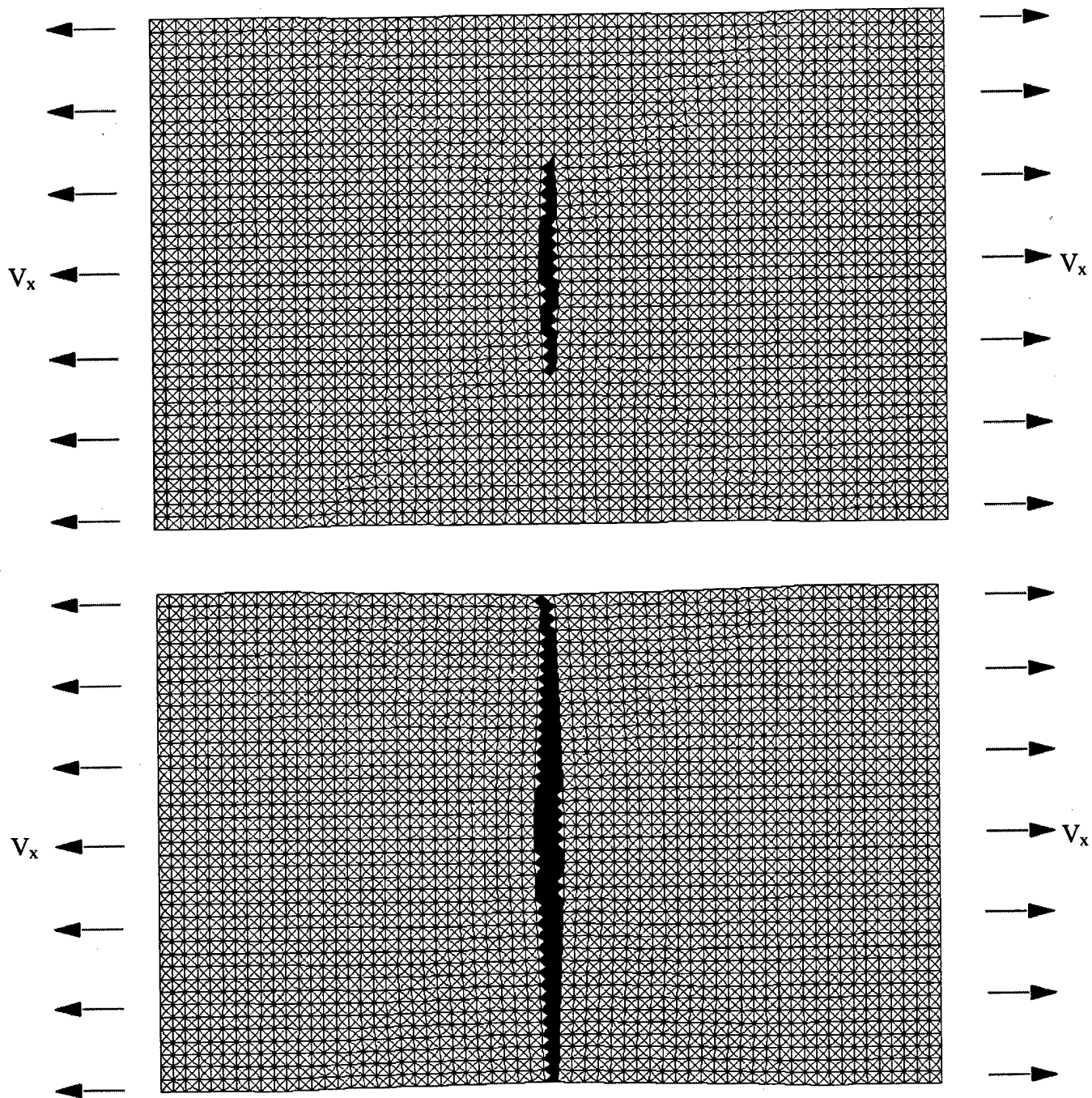
Figure 15. Tensile Specimen Meshes at 150 μs (top) and 200 μs (bottom)
[14a/b_T103794.tif]
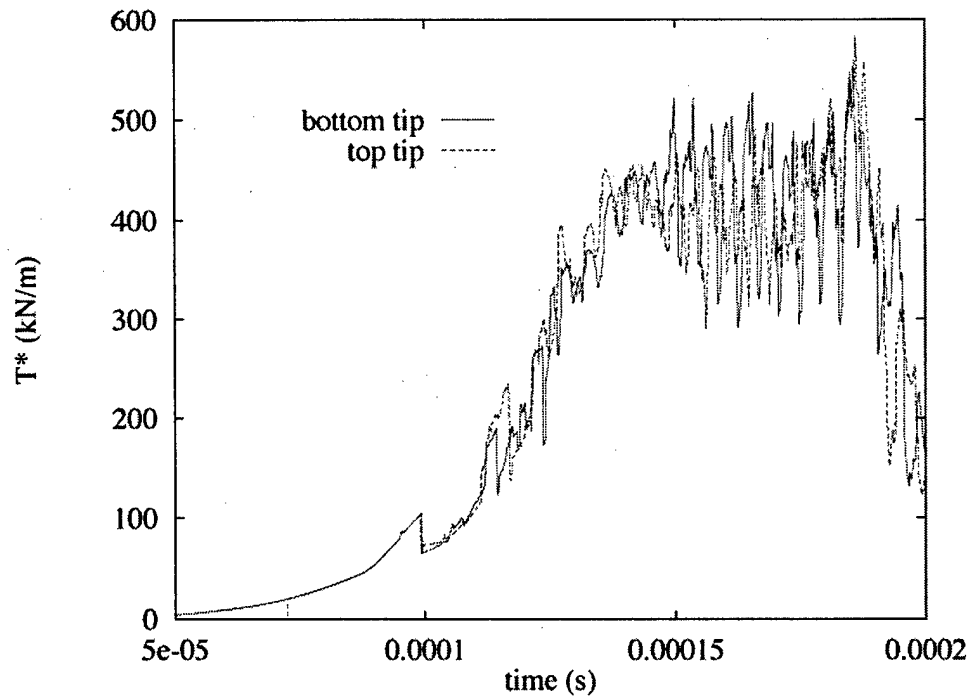
Figure 16. T* Versus Time for Top and Bottom Tips of Interior Crack [15_T103794.tif]

SECTION 3

3D ALGORITHM

This section describes an extension of the 2D algorithm to thin structures in three dimensions. Computations are then presented to compare the accuracy of the algorithm to a node-splitting technique. Also, the fracture of a thin-walled cylinder loaded in torsion is simulated to demonstrate the three-dimensional capability.

3.1 THE 3D ELEMENT-FAILURE ALGORITHM

Figure 17 demonstrates methods of modeling cracks with finite elements. The top left of the figure depicts a node-splitting representation of a crack in two dimensions. For this type of representation, the newly formed crack faces are modeled by contact surfaces, necessitating remeshing around the crack tip.

The top right of Figure 17 depicts a crack represented by the element-failure technique in two dimensions, as described in Section 2. The crack tip is tracked through the mesh, and elements are failed as the tip passes through them. Failed elements support no deviatoric or tensile volumetric stresses, modeling frictionless crack faces along their boundaries with unfailed elements. It can be seen in Figure 16 that each node remains attached to at least one unfailed element as the crack tip moves through the mesh.

The extension of this element-failure algorithm to three dimensions is depicted at the bottom of Figure 17. The extension is not fully general; it is assumed that the structure contains one small thickness relative to the other dimensions, and that the crack front spans this thickness. These restrictions logically permit the computation of one value (averaged over the length of the crack front) of the fracture energy per unit area of new crack face, T^*, and one direction of propagation. All points along the crack front are therefore restricted to propagation at the same rate in the same direction. The structural thickness, however, need not be uniform.
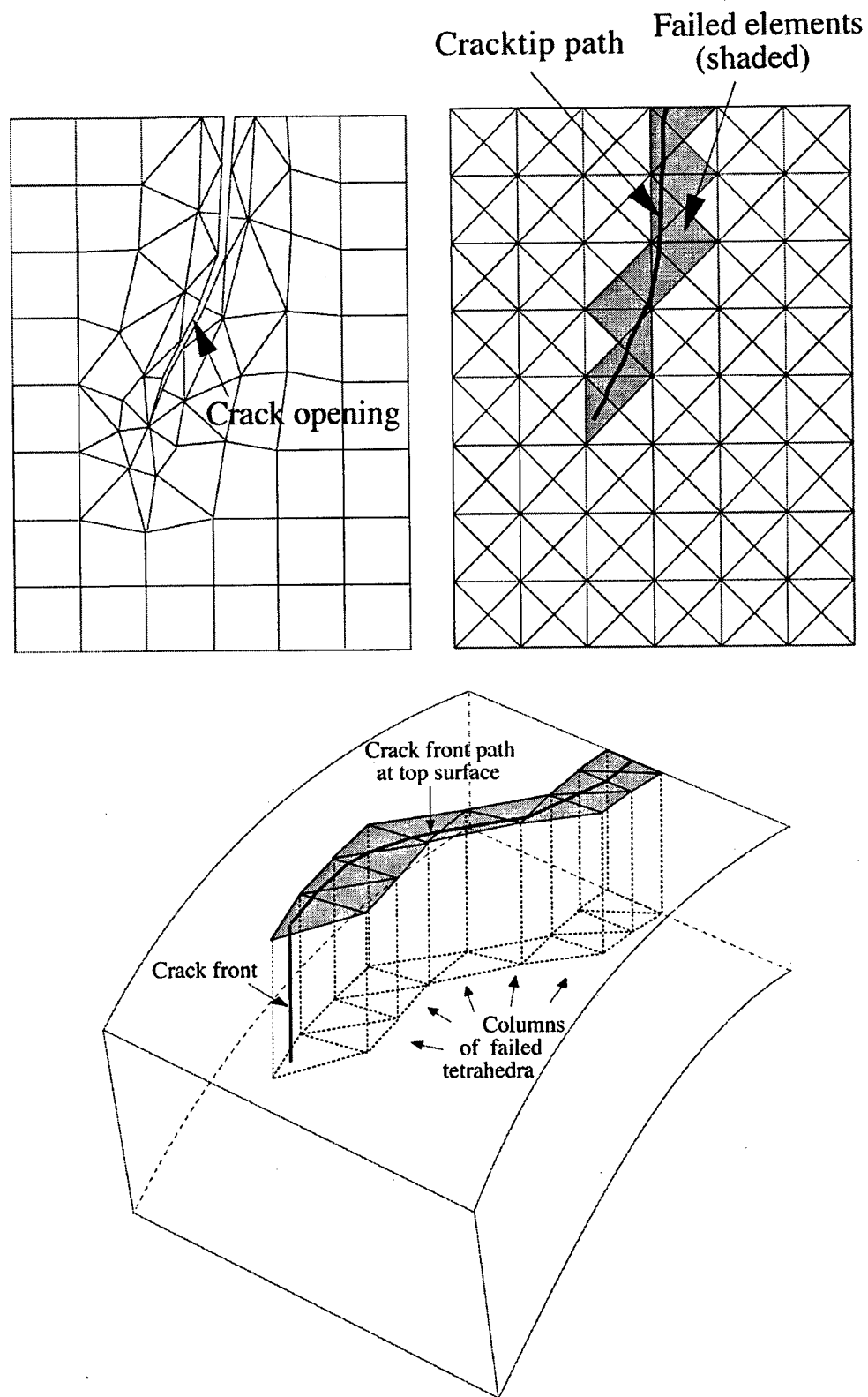
Figure 17. Methods of Modeling Cracks with Finite Elements: 2D Node Splitting (top left), 2D Element Failure (top right) and 3D Element Failure (bottom, unfailed elements not shown)

To most accurately model a crack front of uniform speed and direction of propagation, the elements must be aligned in columns through the thickness of the structure, as shown at the bottom of Figure 17. A direct benefit of this element arrangement is that the element-failure algorithm introduced for planar models can be applied to the surface of the 3D structure in a straightforward manner. The extension to three dimensions is then reduced to including the effects of the elements that are aligned with the top-surface elements in the routines applied to the top surface. Such an implementation will be described in the following two subsections.

Under the current restrictions (a thin 3D structure with a crack front of uniform speed and direction of propagation spanning the thin dimension), it would also be appropriate to model the 3D structure with shell elements and apply the 2D element-failure method directly to the shell elements. The approach of using solid elements aligned in columns through the thin dimension of the structure is used here due to the ease with which the solid elements can be attached to other parts of the structure which do not possess a thin dimension and must be modeled by solid elements. An example of such a geometry is that of the steel case of a hard target penetrator.

3.1.1 Fracture Model

The bottom of Figure 17 demonstrates a trail of failed elements traversed by a crack front, and how the failed elements model a crack. To simulate the flaw required to initiate fracture, the algorithm fails a column of elements specified by the user. If this flaw lies on an edge of the structure, one value of T* is calculated and a corresponding crack front may propagate through the structure, simulating an edge crack. If the flaw is not on an edge, two values of T* are calculated and two corresponding crack fronts may propagate, simulating an internal crack.

The "top" surface of the structure denotes the surface on which the planar element-failure algorithm is applied. The intersection of the crack front and the top surface is used to define the crack path, as in Figure 17. The path is restricted to travel in a straight line across each element face. On the timestep during which it enters a new element face, a routine to determine the new direction of propagation is invoked. In this section, the direction of propagation is taken as the direction normal to the maximum principal stress (mode I fracture) for a state of stress that is obtained by averaging the stresses along the crack front. While the direction of propagation is only updated when the crack front enters a new column of elements, the fracture energy is calculated at each timestep, and — combined with the fracture criterion — it updates the speed of propagation.

Although the crack path is defined on the top surface of the structure, it represents the history of the entire crack front. Due to the alignment of elements in columns through the thickness, when the crack path enters a new element face, the crack front simultaneously enters a new column of elements. An important consequence is that all elements through the thickness can be failed simultaneously, maintaining a good approximation to a crack front of uniform speed and direction of propagation.

The failed elements are not permitted to support deviatoric or tensile volumetric stresses, and they can be realized by simply modifying their constitutive relations so that they can sustain only positive pressure, typically occurring under negative volumetric strains. When an element is failed, its stresses are set to zero and their effect is replaced by externally applied nodal forces that are equivalent to the internal nodal forces contributed by the element stresses before zeroing. These external nodal forces are reduced to zero linearly as the crack front traverses the element. They reduce the release waves associated with the sudden failure of elements [7, 8, 9] and extract energy from the structure. A surface between a failed and an unfailed element acts as a traction-free crack face when the volumetric strain of the failed element is positive (opened crack), and a pressure-transmitting crack face when the volumetric strain of the failed element is negative (closed crack).

3.1.2 The T* Fracture Parameter

As a measure of the energy release associated with a unit area of crack surface extension in dynamic fracture, T* [17, 18] is expressed as,

$$T^* = \lim_{\Gamma^* \to 0} \int_{\Gamma^*} \left[\left(\overline{W} + T \right) n_p - \sigma_{ij} n_j u_{i,p} \right] d\Gamma^* \tag{4}$$

which is identical to Equation 1 for 2D geometry, except that Γ^* is now a surface contour around the crack front. $\overline{W}$ and T represent the internal energy density and kinetic energy density, respectively; σ_{ij}, the ij-th component of the stress tensor; n_j, the j-th component of the unit normal vector to Γ^*; n_p, the component of the unit normal vector in the direction of crack propagation; u_i, the i-th component of the displacement vector; $u_{i,p}$, the derivative of the i-th component of the displacement vector in the direction of crack propagation.

The largest errors in a numerical solution occur in the region of the crack front where field quantities vary most rapidly. As a result, it is again desirable to equate the limiting integral of Equation 4 to volume and surface integrals by the divergence theorem [7],

$$T^* = \int_\Gamma \left[\left(\overline{W} + T \right) n_p - \sigma_{ij} n_j u_{i,p} \right] d\Gamma - \int_\Omega \left[\left(\overline{W} + T \right)_{,p} - \rho \ddot{u}_i u_{i,p} - \sigma_{ij} \left(u_{i,j} \right)_{,p} \right] d\Omega \qquad (5)$$

where Γ represents a far-field crack-front surface contour and Ω is the volume between Γ and Γ^*. Here, n_j is the j-th component of the unit normal vector to Γ. (A subscript following a comma represents the direction of a spatial derivative.)

The top of Figure 18 shows an example of the domains of Γ, Γ^* and Ω for the calculation of T^* in a planar model, and the bottom of Figure 17 shows them (without elements) about a crack front spanning the thin dimension of a structure. Although T^* is defined over Γ^* in the limit as it is shrunk about the crack front (Equation 4), only the domains of Γ and Ω are used in the computations (Equation 5).

To determine which elements comprise Ω and which element faces comprise Γ, the algorithm developed for the planar models can be applied to the element faces of the top surface. In this way, the distance R between the centroid of each top-surface element face and the crack front at the top surface is compared to nominal values of the radius of Γ^*, R_{Γ^*}, and the radius of Γ, R_Γ. If R lies between the two, $R_{\Gamma^*} \leq R \leq R_\Gamma$, then the top-surface element and all elements aligned with it are included in Ω. Figure 19 depicts this comparison for one top-surface element and the elements aligned with it.

Once the comparison has been made for all top-surface elements and the domain Ω has therefore been established, the element faces of Ω are then categorized as either members of Γ^* or Γ. Those that define the crack-front surface contour belong to Γ^*; all others belong to Γ. It has been recommended [7, 8] that all elements that have been inside Γ^* be excluded from Ω in subsequent evaluations of T^* due to the lack of accuracy of the numerical solution in the crack-front region and the continuation of those errors when path-dependent materials (plasticity) are unloaded. The result is a zone of elements that are not included in Ω forming a wake behind the crack front. The boundary of this exclusion zone defines Γ^*.
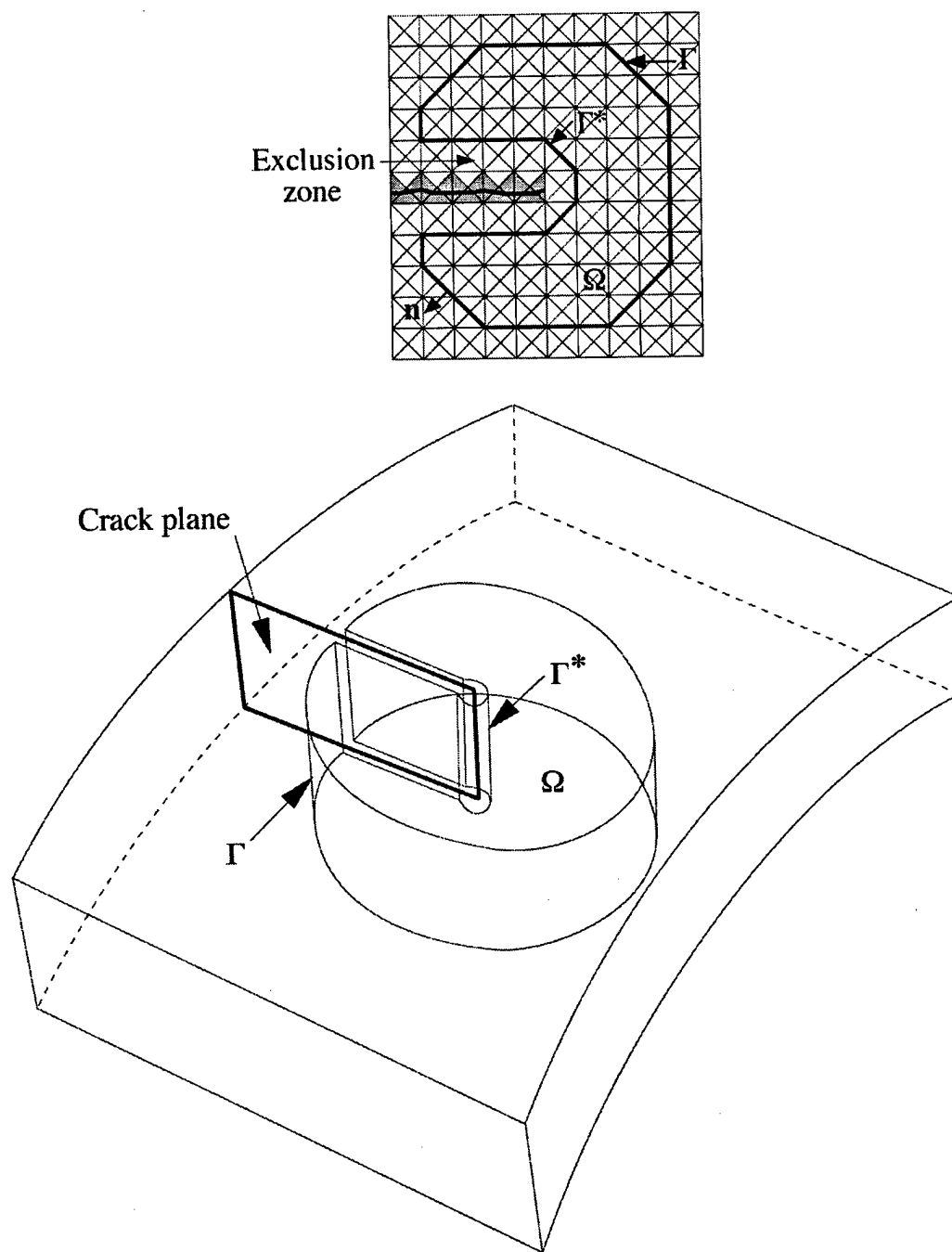
Figure 18. Domains in the Definition and Calculation of T* for 2D (top) and 3D (bottom, elements not shown)
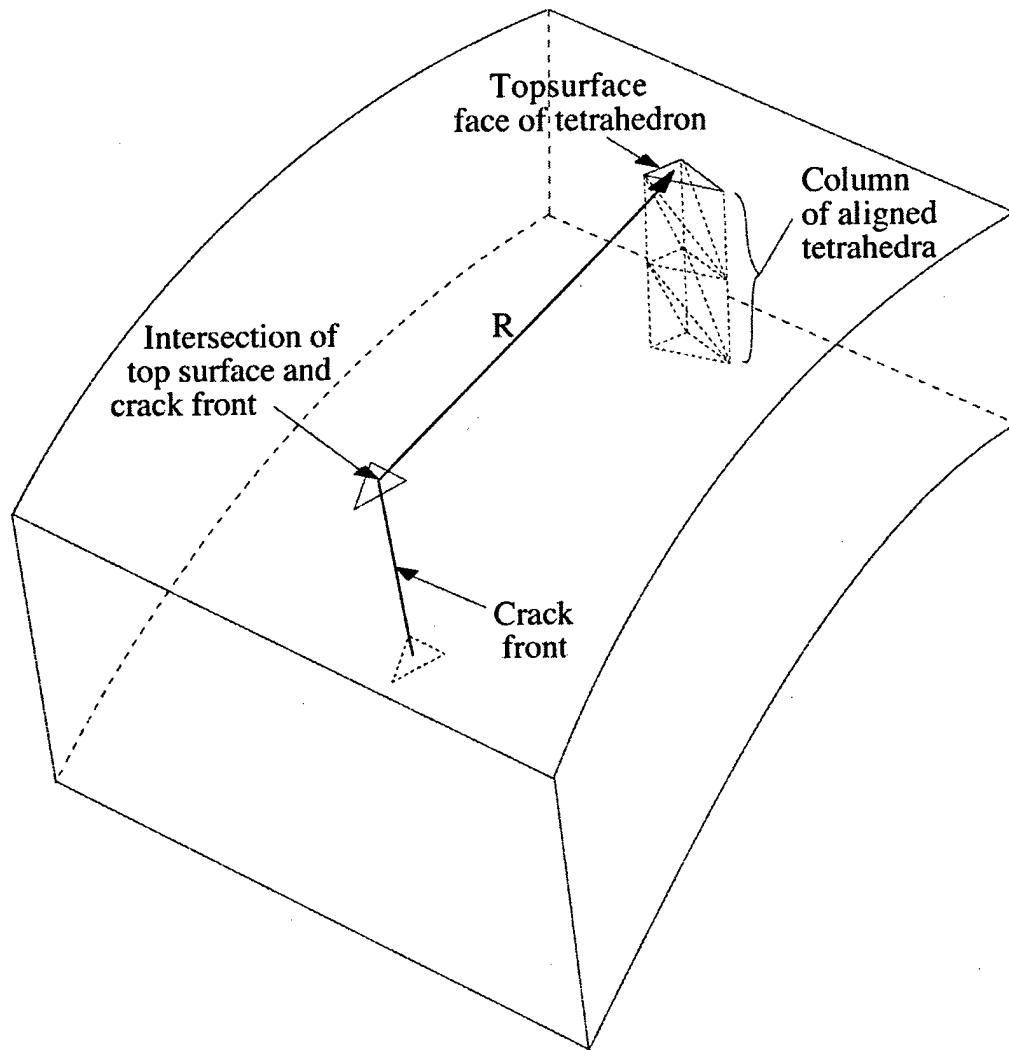
Figure 19. Distance from Crack Front for Candidate Elements of Ω

Across each tetrahedral element, the displacement is interpolated linearly, resulting in constant displacement derivatives, stresses, densities, and internal energy densities. Numerical integration of the integral over Γ in Equation 5 is therefore achieved by one-point integration on each of the boundary surfaces.

The integral over Ω in Equation 5 is integrated by employing one-point quadrature over each tetrahedral element in Ω. For constant-strain tetrahedra, the second-order displacement derivatives must be smoothed before application of the quadrature scheme (because they are zero in the interiors of the elements and infinite at the element boundaries). Smoothing is achieved by averaging values of the first displacement derivatives from the adjoining elements at each node, and then interpolating those nodal values linearly over each element to render constant second

displacement derivatives in each element. A similar approach is used for the energy-density derivatives.

It has been demonstrated [8] that a lack of convergence with mesh refinement occurs for solutions of ductile fracture if $R_{\Gamma*}$ is taken as the limit value of zero. For this reason, the computations of the following section were performed with a value of $R_{\Gamma*}$ just large enough to exclude one or two columns of elements on all sides of the crack front from Ω.

3.2 NUMERICAL RESULTS

As noted previously, the 3D algorithm has been incorporated into the 1999 version of the EPIC code [2, 19]. In the example computations that follow, the direction of propagation is taken normal to the maximum principal stress.

3.2.1 Comparison of 3D Element Failure and 2D Node Splitting

The primary advantage of the element-failure method is the simplicity of implementation. This subsection is intended to demonstrate its accuracy. It has been shown in Section 2, by the comparison of coupled pressure-bar simulations, that the accuracy of the element-failure method presented for planar problems is similar to that of the node-splitting method. Here, the same coupled pressure bar will be modeled in three dimensions and results will be compared to plane-strain node-splitting results.

The coupled pressure bar experiment is depicted in Figure 20. The geometry is identical to that used for the 2D computations in Section 2, except that the 3D geometry requires a specified thickness. The material model and loading are identical to those used for the 2D problem in Section 2.

The mesh of the node-splitting algorithm is shown on the left side of Figure 21, and it contains 1419 nodes and 2720 elements. Symmetry allows the modeling of half the specimen, and node "splitting" is achieved by releasing nodes along the line of symmetry, replacing each restraint by an external nodal force that is equivalent to the internal nodal force due to element stresses, and reducing the external forces to zero as the crack tip traverses the element edge (as described in Section 2).
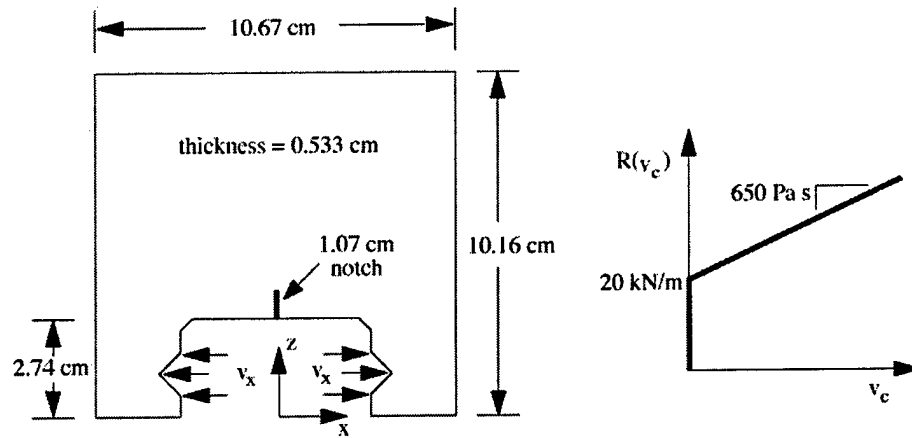
Figure 20. Coupled 3D Pressure-bar Specimen and Fracture Response Function
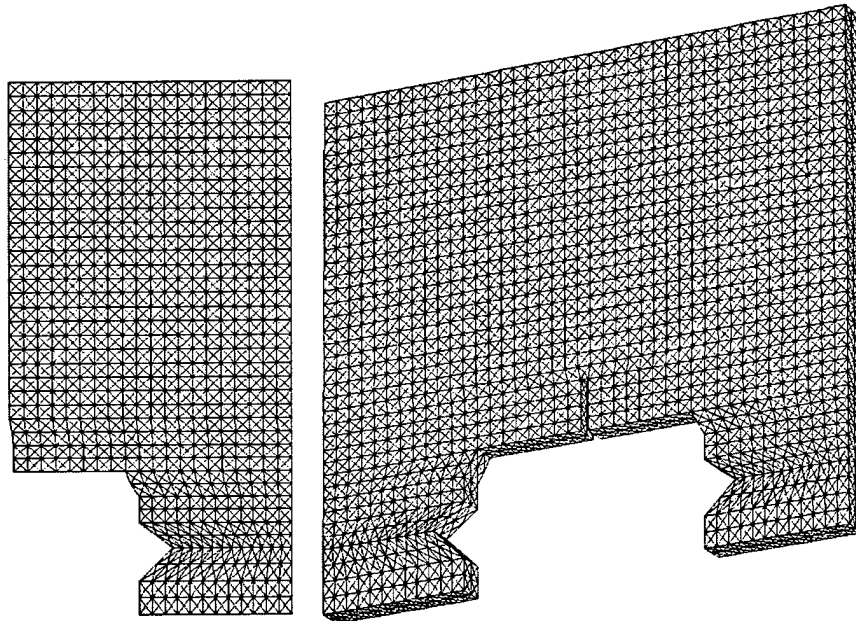
**Figure 21. Meshes for Comparison of 2D Node-splitting (left, 2720 elements) and
3D Element-failure (right, 66,432 elements) Methods**

For the element-failure algorithm in three dimensions, no symmetry assumptions are made and a mesh of 17,076 nodes and 66,432 elements is used, as shown on the right side of Figure 21. The mesh contains 5536 triangular element faces on the top surface, as compared to the 5440 triangular elements represented by the plane-strain node-splitting mesh (left side of Figure 21).

The nodes are restrained from motion normal to the top surface to simulate plane strain conditions. For both algorithms, $R_\Gamma = 1.5$ cm and $R_{\Gamma*} = 0.5$ cm.

Figure 22 contains plots of T* and the z-coordinate of the crack front as functions of time for both the node-splitting and element-failure methods. Similar accuracy of the two methods is reflected in the close agreement of the solutions.
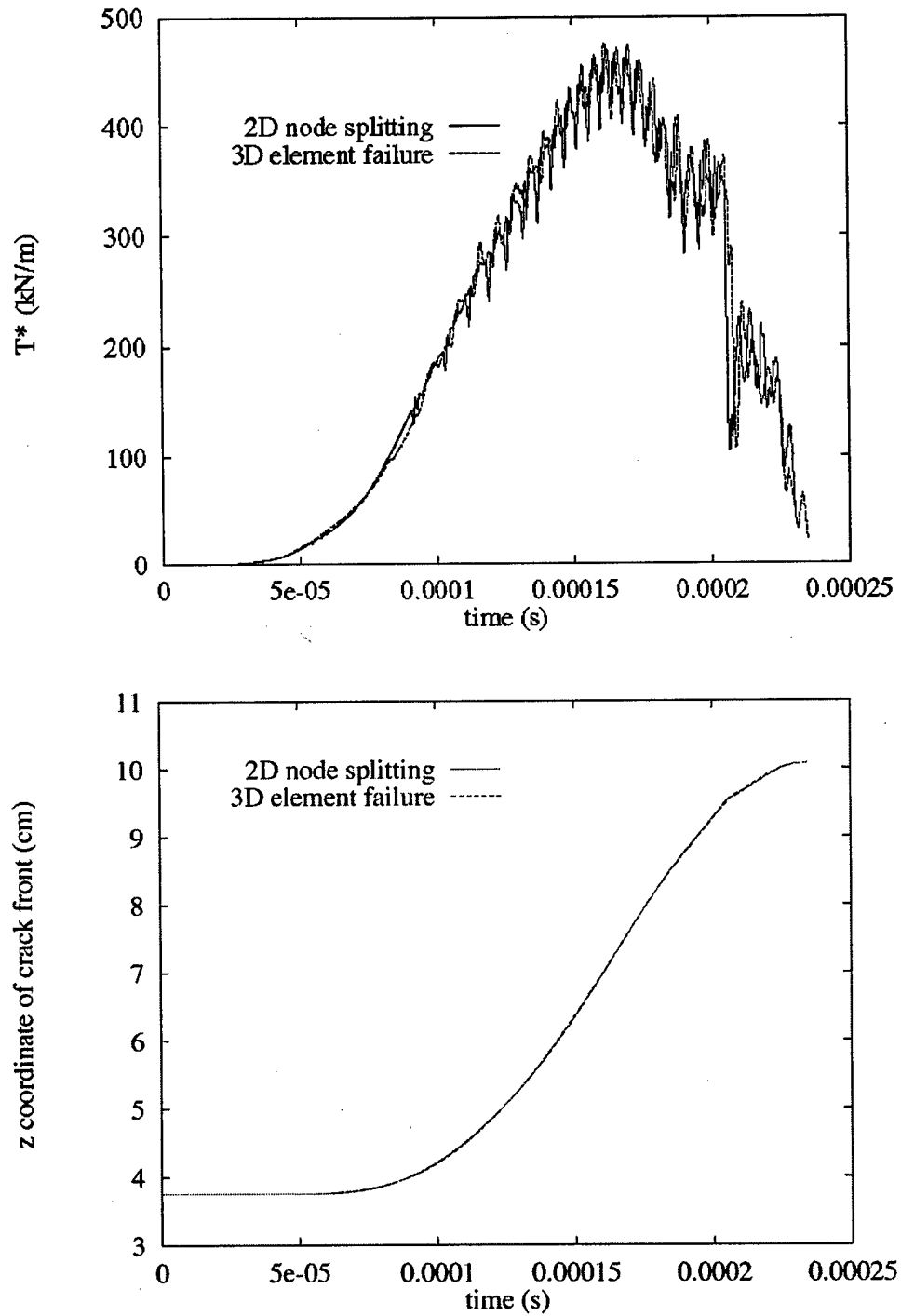
Figure 22. Comparison of Results for 2D Node-splitting and 3D Element-failure Methods

Figure 23 is a plot of the element-failure mesh at 250 μs, with the failed elements darkened. The crack can be seen to propagate up the line of symmetry with little variation.
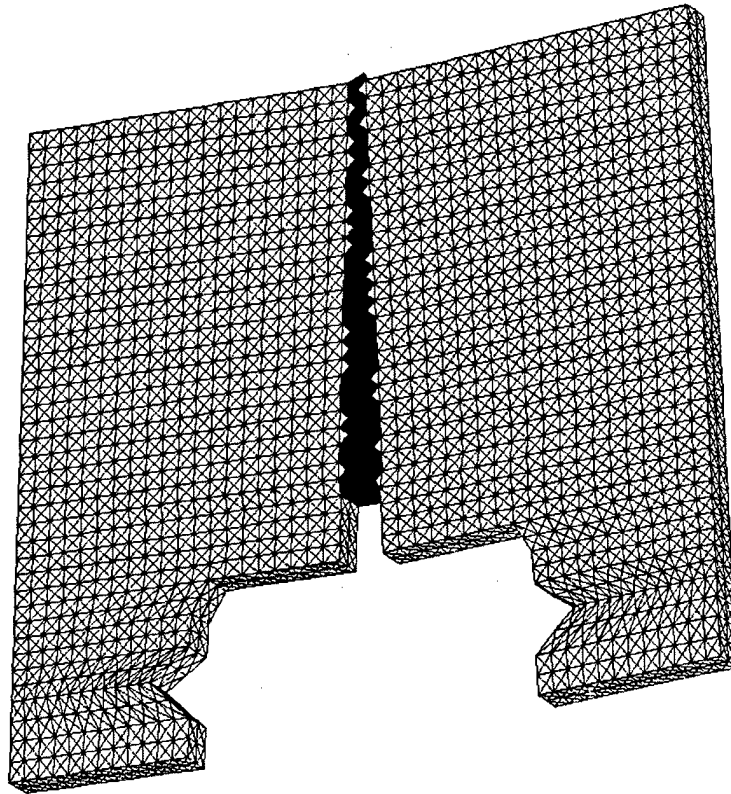
Figure 23. Element-failure Mesh at 250 μs (failed elements darkened)

3.2.2 Fracture of Thin-walled Cylinder under Torsion

The computation in this subsection is intended to demonstrate the three-dimensional capability of the algorithm. The problem consists of a thin-walled cylinder under torsional loading. One end of the cylinder is restrained against motion in the plane normal to the cylinder axis, while the other end is subjected to a rotational velocity, as shown in Figure 24. Both ends are free to deform in the axial direction.

The elastic/perfectly plastic material model of the previous subsection is also used for these computations. The mesh is composed of 20,376 nodes and 69,120 tetrahedral elements, as shown on the left side of Figure 25. An initial flaw in the material is simulated by failing a column of elements near the midlength of the cylinder. This column is darkened in the plot on the left side of Figure 25. In the computations of T^*, $R_\Gamma = 1.5$ cm and $R_{\Gamma*} = 0.5$ cm.
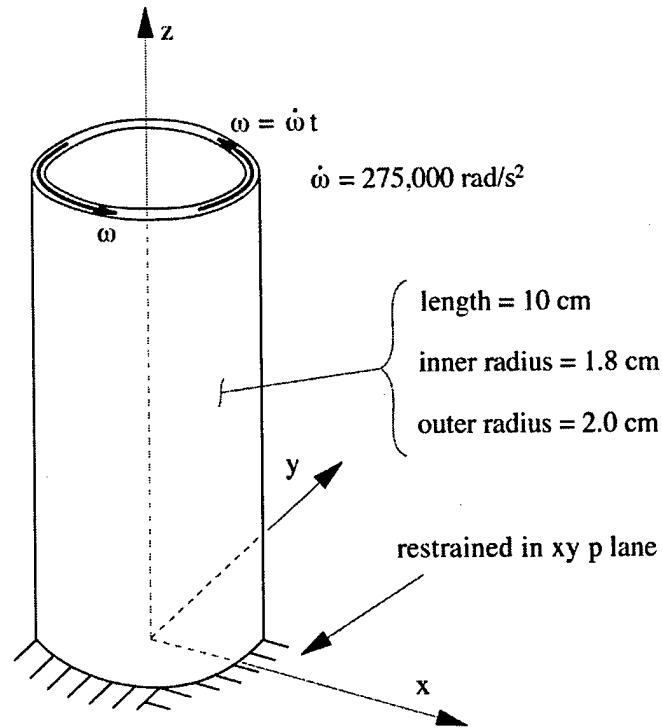
Figure 24. Thin-walled Cylinder Subjected to Torsional Loading
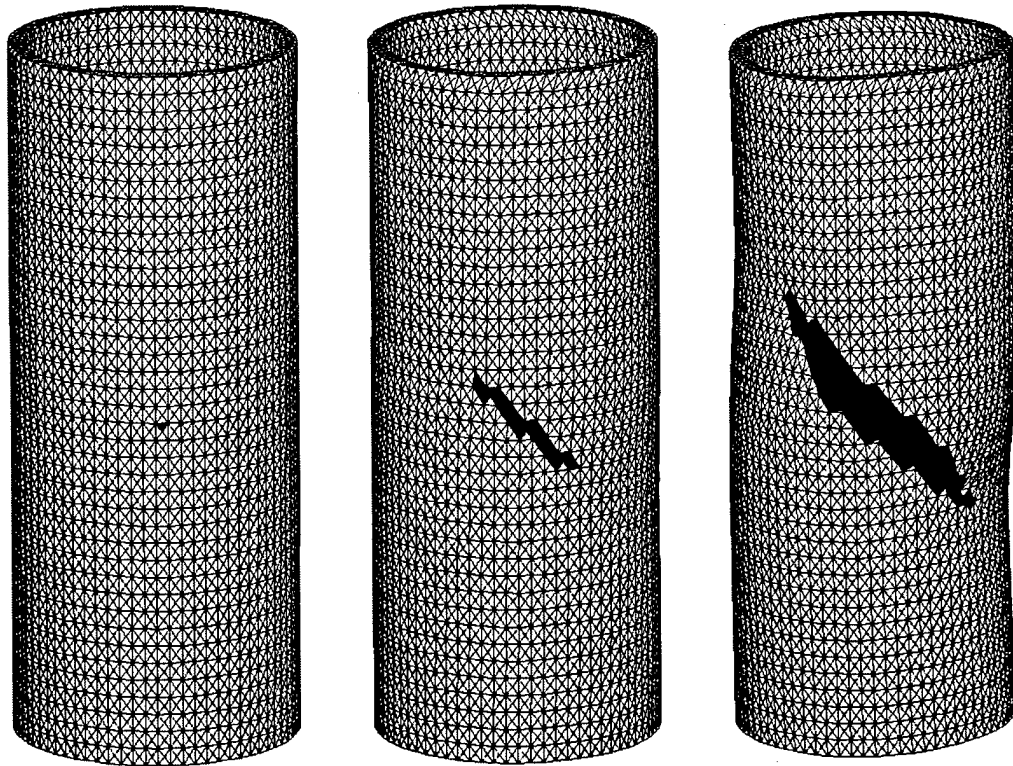
Figure 25. Thin-walled Cylinder Mesh at 0 μs (left) 325 μs (center), and 400 μs
(right). Failed elements are darkened, including the initial flaw at left.

After 325 µs of loading, two crack tips have begun to propagate in opposite directions from the flaw. The plot at the center of Figure 25 shows the mesh at this time, with failed elements darkened. After 400 µs, the crack tips have propagated farther, as shown on the right side of Figure 25, and the crack is opening in mode I. Only those elements through which the crack front has passed have been failed. The increased width of the crack at 400 µs is represented by the failed elements that are allowed to freely deform under the zero stress state associated with expanded failed elements.

SECTION 4

PARAMETRIC COMPUTATIONAL STUDY

The final objective for this work is to have the capability to perform 3D crack propagation computations for penetrators impacting a variety of hard concrete targets. The series of parametric computations that follows demonstrates this capability.

A description of the configuration used for the parametric computations is shown in Figure 26. The initial flaw positions occur at points A, B, C, and D. The geometry and impact conditions of the generic hard target penetrator are similar to that presented previously by Johnson, et. al. [20]. The penetrator has a length of L = 203 cm and a diameter of D = 25.4 cm, for L/D = 8. The length of the nose is 63.5 cm and the wall thickness is 2.54 cm. The case material is 4340 steel with a hardness of R_c49. A characterization of this material for the Johnson-Cook strength model is provided in [21], and it is represented by material number 85 in the EPIC material library. The inert explosive is Filler E, represented by material number 60 in the library. The total weight is 366 kg.

The penetration is represented by 65,736 tetrahedral elements. The inert explosive and the penetrator case utilize the elements in a symmetric arrangement (24 tets per brick), and the steel nose uses a nonsymmetric arrangement (6 tets per brick). Symmetric bricks were used for the case because it was determined that the crack propagation computations were sometimes more accurate and robust with this arrangement. The newly developed uniform ring option for rod shapes (in the EPIC preprocessor) was used to meet the through thickness assumptions in the algorithm. The nonsymmetric brick arrangement was used in the nose because there is no current capability to generate symmetric bricks with a uniform ring arrangement for nose shapes. Also, the entire penetrator (without a plane of symmetry) is included in the model because the crack propagation algorithm cannot accurately account for planes of symmetry. Furthermore, after a crack begins to form there is no longer a plane of symmetry.

The crack propagation model (crack propagation velocity versus T*) is discussed and presented in Part 1 of this report [1]. The relationship between T* and crack velocity is also included in Figure 26.

The concrete target has a compressive strength of $f'_c = 34.5 \, \text{MPa} \, (5000 \, \text{lb/in}^2)$, and a density of $2280 \, \text{kg/m}^3$. It is assumed to be infinitely thick and infinitely wide. The resistance of the target is represented by the PENCRV3D model that is linked to the finite element representation of the penetrator [2]. This simplified representation of the target allows the computations to be run much faster (hours instead of days of CPU time), such that parametric computations can be performed.

Figure 27 shows the dynamic response of the baseline computation, in which cracks are excluded. At 2.0 ms the penetrator is loaded such that bending introduces compression in the forward wall of the penetrator and tension in the aft wall. At 5.0 ms the penetrator straightens to approximate the original configuration, and at 10.0 ms it has almost stopped.

Figure 28 shows the computed response for the initial flaw at point A. At a time of approximately 1.5 ms, T* begins to rise for both fronts and the crack propagates. At about 2.3 ms T* for both fronts goes negative and the crack no longer propagates. At 2.8 ms T* for the aft front goes positive and the computation stops because the prescribed array size for the number of cracked elements is exceeded.

Figure 29 shows the computed response for a flaw at point B. Here the crack propagates under the positive T* that occurs between 1.5 and 2.0 ms. When the aft crack tip reaches the base plate of the penetrator it can no longer propagate. The computation continues, however, out to the full 10.0 ms.

Figure 30 shows the response for a flaw at point C. Here a large value of T* is computed and the crack propagates rapidly. For this condition the computation is discontinued at 2.1 ms. A probable explanation is that the reversal in loading tends to change the direction of the crack such that it tries to propagate back into the previously cracked elements. The algorithm in the code cannot currently handle this condition, and the computation is discontinued when this occurs.

Figure 31 shows the response for a flaw at point D. The location of this flaw is essentially under compression and does not propagate significantly because T* is generally negative. Again, it is probable that the reversal of loading is what caused this computation to stop at 4.7 ms. It is interesting to compare and contrast the propagation at point C (extensive propagation in a tensile field) to that at point D (little propagation in a compressive field).

It is difficult to assess the accuracy of these computations because there are no known test data and/or analytic/computational solutions for curved surfaces under reversing loading conditions. The computed values of T* are generally very high and produce more crack propagation than would be expected.

Several questions that need to be answered are as follows:

- What is the effect of curvature.
- What is the effect of zoning.
- What is the effect of general loading that may reverse (and is not always increasing).
- What is the effect of through thickness variations in stress and strain.
- What is the effect of the ratio of the case radius to the case wall thickness.
- What is the effect of the ratio of the case radius to the T* outer radius, Γ.

Future work should address these issues such that the accuracy and/or robustness of the algorithm can be better evaluated and/or improved for hard target penetrator applications.

$V_0 = 305$ m/s at 20° from normal

B

L = 203 cm
D = 25.4 cm
L/D = 8
Case Material: 4340 Rc 49

A

D

C

65,736 Elements

R (kN/m)

70

14
12.5

300   565

V_c (m/s)

Concrete Target (PENCRV3D)
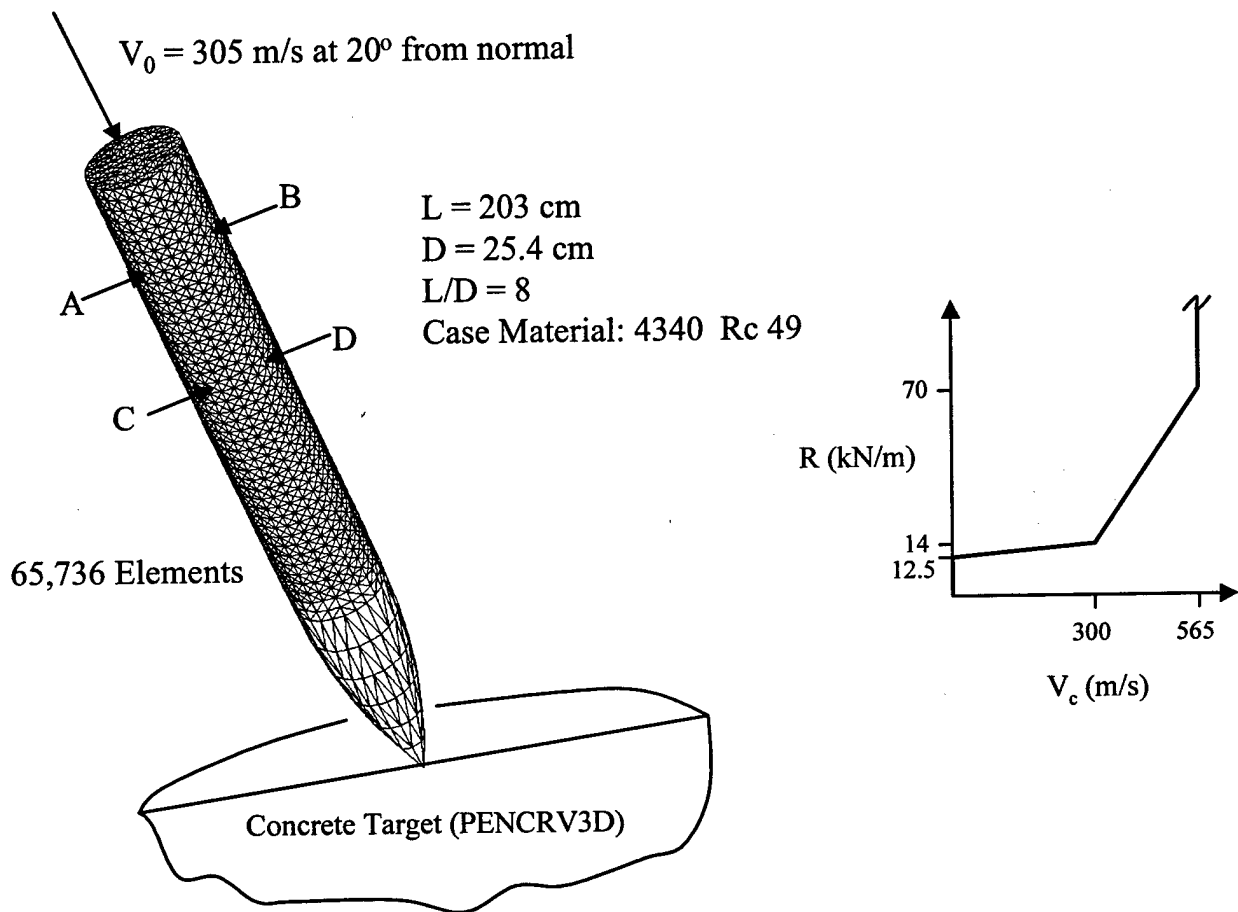
Figure 26. Description of the Parametric Computations

t = 0 ms

t = 2 ms

Concrete surface

t = 5 ms

t = 10 ms
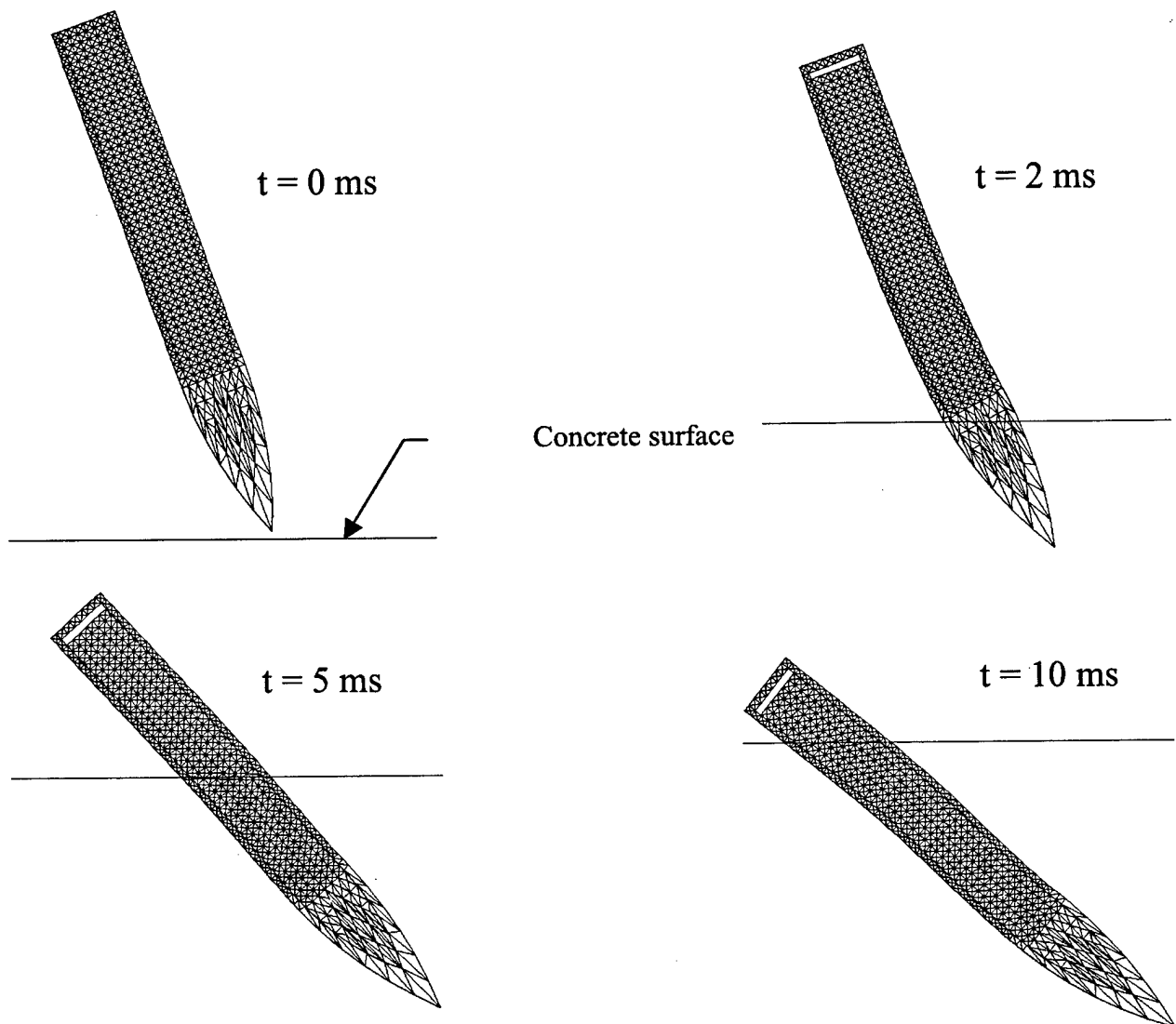
Figure 27. Baseline Computation with No Cracks

t = 2.8 ms

Cross-section   External View
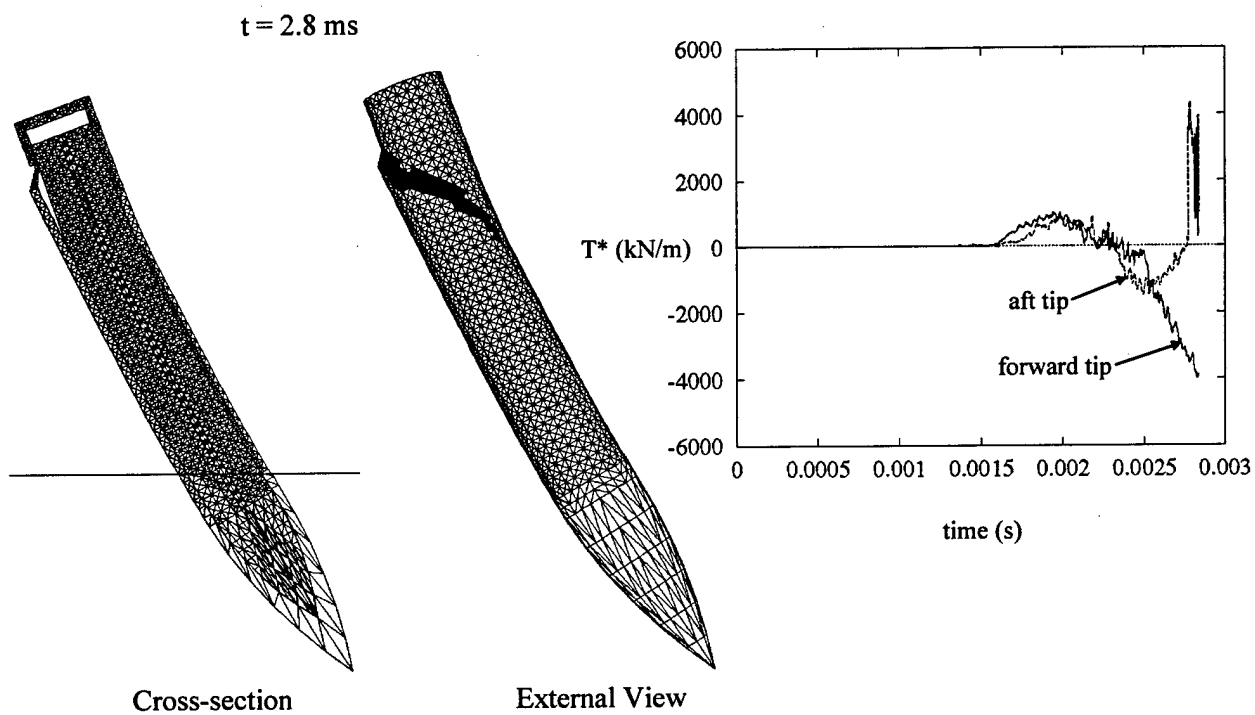
Figure 28. Computation for Initial Flaw at Point A

t = 10 ms

Cross-section

External View

T* (kN/m)

5000

0

-5000

-10000

-15000

aft tip

forward tip

0   0.002   0.004   0.006   0.008   0.01

time (s)
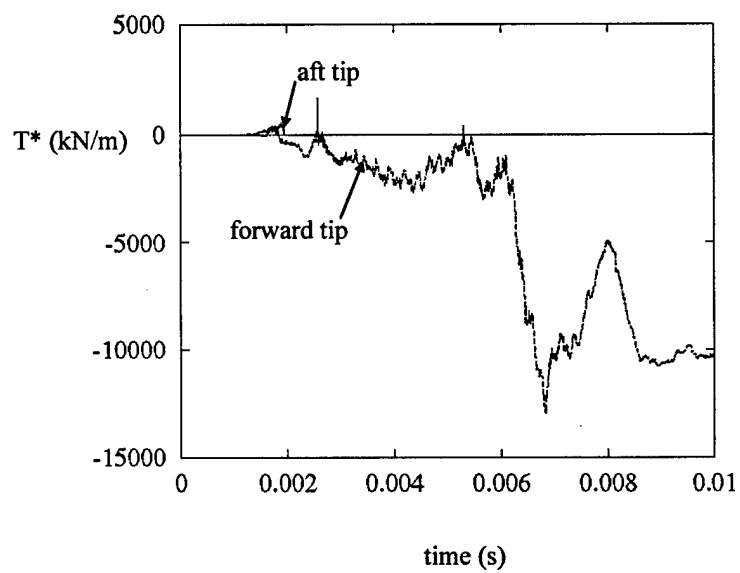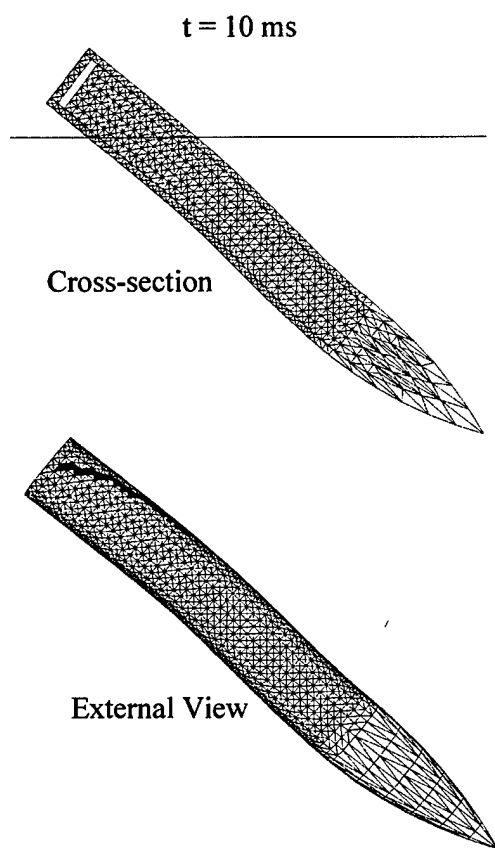
Figure 29. Computation for Initial Flaw at Point B

t = 2.1 ms

Cross-section   External View
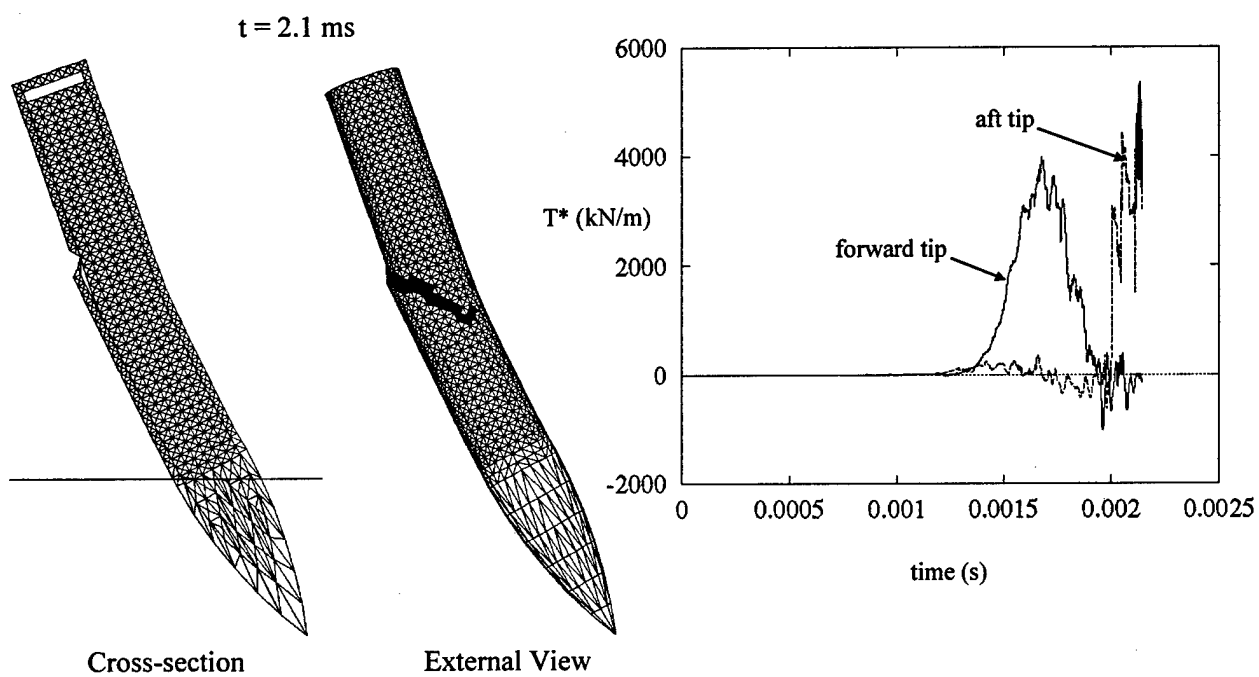
Figure 30. Computation for Initial Flaw at Point C

t = 4.7 ms

Cross-section   External View
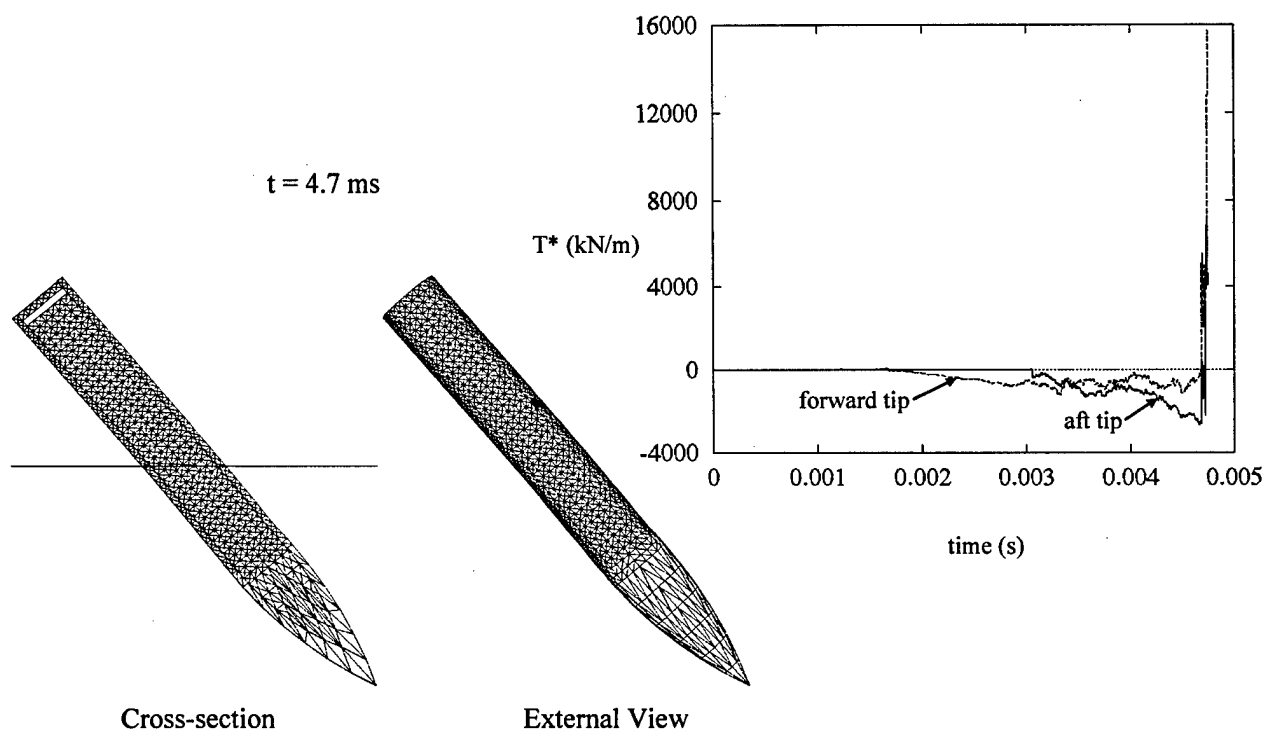
Figure 31. Computation for Initial Flaw at Point D

SECTION 5

SUMMARY AND CONCLUSIONS

This report has provided 2D and 3D crack propagation algorithms for general directions, as well as parameteric crack propagation computations for a penetrator impacting a hard concrete target.

The element-failure method of modeling crack propagation assimilates the fracture mechanics of node-splitting methods with the simplicity of micromechanically based methods. The T* fracture parameter, a measure of the energy release associated with the creation of a unit area of fracture surface under dynamic loading represents a fracture mechanics approach to crack propagation. The technique of failing elements eliminates the need to remesh around the crack tip and redefine contact surfaces.

Numerical examples show similar accuracy of the node-splitting (node-release, along a line of symmetry) method and the element-failure method for meshes of similar refinement. Convergence studies verify the need for a nonzero size of the contour Γ^*, used in the evaluation of T^*, for both methods. Convergence with mesh refinement is lost if the size is zero. The direction of propagation of the element-failure method is chosen as the direction normal to the maximum stress, or the direction of the maximum value of T^*. The ability of the element-failure method to model interior cracks is demonstrated assuming the existence of an initial element-sized material flaw.

The most important characteristic of the element-failure method is that it allows for three dimensional computations to be performed without rezoning. The 3D algorithm has been shown to provide good agreement with 2D computations, and to provide the capability to propagate cracks in general directions. Although the 3D algorithm has provided accurate and robust behavior for flat plates, the application to curved surfaces and changing loading directions has raised some questions that have not yet been fully resolved.

Finally, the 3D algorithm has been successfully applied to the application of a penetrator impacting a hard concrete target.

REFERENCES

1. C.E. Anderson, C.H. Popelar, J.D. Walker, G.R. Johnson, and S.R. Beissel, *Penetrator Case Fracture Predictive Technology: Volume 1 – Analysis and Test Data,* Report AFRL-MN-EG-TR-xxxx to Air Force Research Laboratory (1999).

2. G.R. Johnson, R.A. Stryk, and S.R. Beissel, *User Instructions for the 1999 Version of the EPIC Code*, Alliant Techsystems Inc., Hopkins, MN, 1999.

3. M. S. Shephard, N. A. B. Yehia, G. S. Burd and T. J. Weidner, "Automatic Crack Propagation Tracking," *Composite Structures* **20**, 211–223, (1985).

4. Y. Sumi, "Computational Crack Path Prediction," *Theoretical and Applied Fracture Mechanics* **4**, 149–156 (1985).

5. T. Nishioka, R. Murakami and S. Matsuo, "Finite Element Simulation of Fast Curving Fracture Tests," *Proceedings of International Conference on Computational Engineering Science*, (Edited by S. N. Atluri *et al*), 750–755 (1991).

6. I. L. Lim, I. W. Johnston and S. K. Choi, "A Finite Element Code for Fracture Propagation Analysis within Elasto-plastic Continuum," *Engineering Fracture Mechanics* **53**, No. 2, 193–211, (1996).

7. F. W. Brust, T. Nishioka, S. N. Atluri and M. Nakagaki, "Further Studies on Elastic-plastic Stable Fracture utilizing the T* Integral," *Engineering Fracture Mechanics* **22**, No. 6, 1079-1103, (1985).

8. R. J. Dexter and P. E. O'Donoghue, "Computational Procedures and Energy Integral for Dynamic Fracture in Viscoplastic Materials," *Engineering Fracture Mechanics* **44**, No. 4, 591–607, (1993).

9. R. H. Dodds, Jr., M. Tang, and T. L. Anderson, "Numerical Procedures to Model Ductile Crack Extension," *Engineering Fracture Mechanics* **46**, No. 2, 253–264, (1993).

10. A. Needleman and V. Tvergaard, "Mesh Effects in the Analysis of Dynamic Ductile Crack Growth," *Engineering Fracture Mechanics* **47**, No. 1, 75–91, (1994).

11. G. R. Johnson and W. H. Cook, "Fracture Characteristics of Three Metals Subjected to Various Stains, Strain Rates, Temperatures, and Pressures," *Engineering Fracture Mechanics* **21**, No. 1, 31–48, (1985).

12. T. Belytschko, L. T. Gu and Y. Y. Lu, "Fracture and Crack Growth by Element Free Galerkin Method," *Modeling and Simulation in Material Science and Engineering* **115**, 277–286 (1994).

13. T. Belytschko and M. Tabbara, "Dynamic Fracture using Element-free Galerkin Methods," *International Journal for Numerical Methods in Engineering* **39**, 923–938 (1996).

14. Y. Y. Lu, T. Belytschko and M. Tabbara, "Element-free Galerkin Methods for Wave Propagation and Dynamic Fracture," *Computer Methods in Applied Mechanics and Engineering* **126**, 131–153 (1995).

15. S. N. Atluri, T. Nishioka and M. Nakagaki, "Recent Studies of Energy Integrals and their Applications," Plenary Paper, ICF6 (4-10 Dec. 1984), New Delhi, India, in *Advances in Fracture Research* (Edited by S. R. Valluri, *et al*), pp. 181–210. Pergamon Press, Elmsford, NY (1984).

16. T. Nakamura, C. F. Shih and L. B. Freund, "Computational Methods based on an Energy Integral in Dynamic Fracture," *International Journal of Fracture* **27** 229–243 (1985).

17. S. N. Atluri, "Path-independent Integrals in Finite Elasticity and Inelasticity, with Body Forces, Inertia, and Arbitrary Crack-face Conditions," *Engineering Fracture Mechanics* **16**, No. 3, 341–364 (1982).

18. S. N. Atluri, T. Nishioka and M. Nakagaki, "Incremental Path-independent Integrals in Inelastic and Dynamic Fracture Mechanics," *Engineering Fracture Mechanics* **20**, No. 2, 209–244, (1984).

19. G. R. Johnson, R. A. Stryk, T. J. Holmquist and S. R. Beissel, Numerical Algorithms in a Lagrangian Hydrocode. Report WL-TR-1997-7039 to Wright Laboratory, U. S. Air Force (1997).

20. G. R. Johnson, R. A. Stryk, J. A. Schonhardt, W. H. Cook and J. A. Collins, "Effects of Velocity, Obliquity and Yaw for a Penetrator Impacting Concrete Targets With and Without Reinforcing Steel," *Proceedings of Thirteenth International Symposium on Ballistics*, Stockholm, Sweden (1992).

21. T. J. Holmquist and G. R. Johnson, "Strength and Fracture Characteristics for Three High Strength Steels Subjected to Various Strains, Strain Rates, Temperatures and Pressures," Alliant Techsystems Report for Contract F08630-92-C-0006 (1994).

DISTRIBUTION LIST
AFRL-MN-EG-TR-1999-7054

Defense Technical Information Center   1
8725 John J. Kingman Road, Ste 0944
Ft Belvoir, VA 22060-6218

Southwest Research Institute   3
Attn: Dr. C. E. Anderson
P. O. Drawer 28510
San Antonio, TX 78228-0510

Alliant Techsystems, Inc.   2
Attn: Dr. G. R. Johnson
600 Second Street N. E.
Hopkins, MN 55343

EGLIN AFB OFFICES:

AFRL/CA-N   1
AFRL/MNOC-1 (Tech Library)   1
AFRL/MNA   1
AFRL/MNAC (Dr. Cook)   5
AFRL/MNAC (Dr. Belk)   1
AFRL/MNAC (Dr. Lijewski)   1
AFRL/MNMW (Dr. Dilmore)   1